Deroy et al. *Microsystems & Nanoengineering* (2021)7:93
https://doi.org/10.1038/s41378-021-00322-6

Microsystems & Nanoengineering
www.nature.com/micronano

ARTICLE Open Access

Predicting flows through microfluidic circuits with fluid walls

Cyril Deroy[1,2], Nicholas Stovall-Kurtz[1], Federico Nebuloni[1,2], Cristian Soitu[3], Peter R. Cook[2]✉ and Edmond J. Walsh[1]✉

Abstract

The aqueous phase in traditional microfluidics is usually confined by solid walls; flows through such systems are often predicted accurately. As solid walls limit access, open systems are being developed in which the aqueous phase is partly bounded by fluid walls (interfaces with air or immiscible liquids). Such fluid walls morph during flow due to pressure gradients, so predicting flow fields remains challenging. We recently developed a version of open microfluidics suitable for live-cell biology in which the aqueous phase is confined by an interface with an immiscible and bioinert fluorocarbon (FC40). Here, we find that common medium additives (fetal bovine serum, serum replacement) induce elastic no-slip boundaries at this interface and develop a semi-analytical model to predict flow fields. We experimentally validate the model's accuracy for single conduits and fractal vascular trees and demonstrate how flow fields and shear stresses can be controlled to suit individual applications in cell biology.

Introduction

Flow is important in many biomedical applications, as cell survival and behavior depend critically on it.[1] It is also essential in organ-on-a-chip devices[2–4] where cells are perfused continuously to mimic in vivo conditions and when studying the effects of transient shear stress on cells.[5] Defining flow fields in these systems is thus essential. The aqueous phase in conventional microfluidic devices is typically surrounded by solid walls (made, for example, of polydimethylsiloxane, PDMS), and flows through them can usually be predicted.[6–8] For example, equations based on pipe flow can be adapted for conduits with arbitrary cross-sections[9] and to model vascular circuits with branches of varying widths.[10–13] As solid walls restrict access, open microfluidics are being developed where parts of walls are replaced by interfaces with air or immiscible liquids[14–16] and equations describing rivulet[17] multiphase[18] and droplet-based flows[19] through conduits with free surfaces have been described.

Recently, an open system termed fluid-walled microfluidics was proved to be particularly suited to biomedical applications. Circuits are built using just a cell culture medium and Petri dishes that biologists use daily, in addition to the bioinert cell-friendly and immiscible fluorocarbon FC40; the two liquids sitting in virgin dishes are reshaped into circuits in seconds.[20–22] The medium in these circuits is confined by FC40 walls held by interfacial forces, and aqueous conduits have cross-sectional profiles of segments of circles that morph as pressures change during flow. Although predicting flows through such morphing cross-sections is challenging, asymptotic methods have been introduced and validated using numerical simulations for transient (passively pumped) systems.[23] However, the development of simpler methods and their experimental validation are still necessary. Here, we characterize how fluid walls change during flow through a simple open-ended conduit. Surprisingly, we find that a common medium component—fetal bovine serum (FBS)—induces elastic no-slip boundaries at the

Correspondence: Peter R. Cook (peter.cook@path.ox.ac.uk) or
Edmond J. Walsh (edmond.walsh@eng.ox.ac.uk)
[1]Department of Engineering Science, Osney Thermo-Fluids Laboratory, University of Oxford, Oxford OX2 0ES, UK
[2]Sir William Dunn School of Pathology, University of Oxford, Oxford OX1 3RE, UK
Full list of author information is available at the end of the article
These authors contributed equally: Cyril Deroy, Nicholas Stovall-Kurtz.

© The Author(s) 2021

Open Access This article is licensed under a Creative Commons Attribution 4.0 International License, which permits use, sharing, adaptation, distribution and reproduction in any medium or format, as long as you give appropriate credit to the original author(s) and the source, provide a link to the Creative Commons license, and indicate if changes were made. The images or other third party material in this article are included in the article's Creative Commons license, unless indicated otherwise in a credit line to the material. If material is not included in the article's Creative Commons license and your intended use is not permitted by statutory regulation or exceeds the permitted use, you will need to obtain permission directly from the copyright holder. To view a copy of this license, visit http://creativecommons.org/licenses/by/4.0/.

medium:FC40 interface. We then develop a semi-analytical model that results in a simple power law; it enables the prediction of flow fields and shear stresses throughout a conduit. Finally, we experimentally confirm the accuracy of the model applied to single conduits and complex vascular trees.

Results

Circuit fabrication and operation

Microfluidic circuits are fabricated using a microjet.[20] A thin layer of cell-growth medium (i.e., DMEM) plus 10% fetal bovine serum (FBS) in a virgin Petri dish is overlaid with FC40, and the tip of a needle held by a 3-way traverse (a 'printer') is lowered through the FC40 until it is located just above the medium (Fig. 1a). The needle is filled with FC40 and connected to a syringe pump; then, starting the pump jets FC40 through the medium on to the bottom of the dish, and the submerged jet sweeps some medium aside. As FC40 wets polystyrene better than the medium, some fluorocarbons remain stuck to the bottom. Moving the needle above the dish in the desired 2D pattern creates a fluid FC40 wall on the bottom of the dish. We begin with a simple open-ended conduit (Fig. 1bi), where medium is infused through a dispensing tube/needle inserted through the fluid ceiling of the conduit (Fig. 1biii); it flows down the conduit and out through the open end into the rest of the dish (the sink; Fig. 1ci).

The challenge: predicting the flows when the fluid walls morph

Unlike the solid walls in traditional microfluidic circuits, which have fixed shapes, FC40 walls/ceilings morph during flow above an unchanging footprint. The curvature of confining FC40 walls is determined by interfacial forces and hence can change during flow. As the Bond number is low, the conduits have cross-sections like the segments of circles; the walls are pinned to the surface of the dish along the triple contact-line where the medium, FC40, and polystyrene meet (Fig. 1c). Analogous to horizontal pipe flow, there is a pressure gradient in the flow direction along a conduit, and hence, the fluid walls morph in response to this gradient. The Laplace pressure at any axial position along the conduit is given by $\Delta P_{\text{conduit}} = \frac{\gamma}{R}$ (where γ is the interfacial tension and R is the radius of curvature). As ΔP is inversely proportional to R, a decrease in P results in an increase in R, which translates into a decrease in conduit height (defined as h_{max} in Fig. 1ciii). Thus, the conduit height falls from the input end (high pressure) to the open end (low pressure; contrast the dark blue sections in Fig. 1cii and Fig. 1ciii). Our challenge is to develop a semi-analytical solution that enables the prediction of velocity and shear stress distributions throughout such conduits.

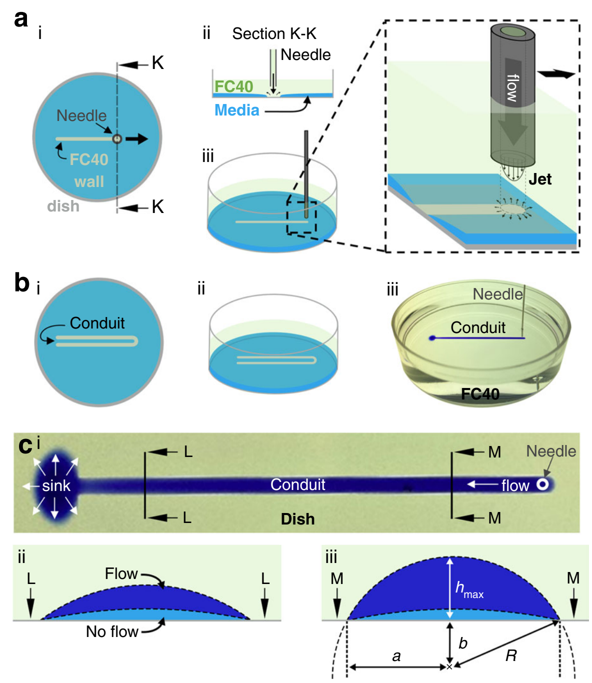

Fig. 1 Workflow. a Building one straight fluid wall by jetting. (i) After wetting a virgin dish with medium and overlaying immiscible FC40, we lower a dispensing needle until it is just above the medium, where it jets FC40 onto the bottom. As the needle moves laterally, the submerged jet sweeps medium aside to leave an FC40 wall pinned to the bottom. (ii) 2D view of Section K-K. (iii) 3D side view of jet. **b** Operation of a simple circuit—an open-ended conduit. (i) 2D and (ii) 3D views of the conduit. (iii) A syringe pump drives dye (added to aid visualization) through the conduit; the dye front has just reached the open end of the conduit and is emptying into the rest of the dish (the sink). **c** Conduit geometry. (i) Top view of the conduit without the needle (position indicated). (ii) Changes in the conduit cross-section at L-L in c(i) during flow. Before flow is initiated, the conduit is bounded by FC40 walls shaped like a spherical cap (light blue). During flow, the walls morph due to the increase in pressure, and the conduit height increases (dark blue). (iii) Changes at M-M. Before flow, the cross-section is similar to that at L-L; during flow, h_{max} increases more than at L-L, as the pressure is higher. R = radius of curvature of the cap. b = distance from the center of the cap to the dish surface. a = conduit half-width.

Measuring the conduit height

As the conduit height reflects the local pressure, we first develop a method to measure it. Medium containing red fluorescent beads is perfused through a conduit sitting on an inverted microscope (Fig. 2a); most beads travel steadily through the conduit, but some remain stationary and stuck to the conduit floor (the dish) or ceiling (the medium:FC40 interface; Fig. 2b). In still photographs taken with the focus on the floor or ceiling, the moving majority appear as blurred streamlines due to the long exposure, and the static minority appear as bright in-focus dots (Fig. 2c). After the distance of a stationary bead stuck to the ceiling from the conduit centerline (z) is measured,

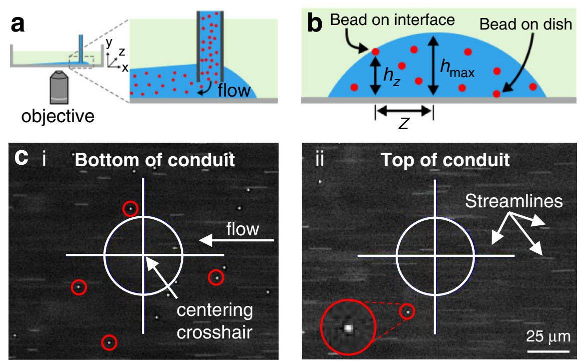

Fig. 2 Experimentally measuring conduit heights. a Overview. The conduit is imaged under a microscope as medium + red fluorescent beads flow through it. **b** Conduit cross-section. Most beads travel down the conduit, but a few are stuck on the bottom or the ceiling. h_{max} is calculated after z (the distance between a bead stuck on the ceiling and the axial centerline in the crosshairs) and h_z are measured using the geometry of a segment of a circle. **c** Images of beads after focusing on the bottom (i) and (ii) top of the conduit. Stuck and stationary beads appear as dots, and moving beads appear as blurs ('streamlines') due to the long exposure.

the conduit height (h_{max}) is calculated using geometry (Fig. 2b) and corrected for refractive effects (Supplementary Information).

FBS creates a no-slip boundary at the medium:FC40 interfaces

As the conduit floor is solid, the no-slip boundary condition applies there and results in zero velocity at the medium:polystyrene interface; therefore, it is unsurprising that beads on the bottom remain stationary (Fig. 2ci). However, it is surprising that some are stationary at the upper interface (Fig. 2cii); we might anticipate that they would be in motion (the viscosity ratio of FC40:medium is ~4). Testing the medium with and without FBS shows that adding serum induces no-slip conditions. As the constitution of FBS is ill-defined and varies from batch to batch, we replace it with the better-defined KnockOut serum replacement (SR) and find that it has the same effect. It was previously shown that cells attach and grow at the interface between fluorocarbon fluids and tissue culture medium.[24,25] As with solid surfaces, cells interact with a monolayer of denatured proteins that adsorb to the interface.[24,25] This monolayer typically consists of serum proteins (in which there is an abundance of albumin); this allow cells to attach and thus presumably induces no-slip conditions in these liquid-liquid interfaces. In our experiments, the medium flows past static FC40, so we change the conditions; FC40 is jetted through FC40 overlaying a static drop containing beads. In the absence of FBS, FC40 flow induces rapid bead motion, as forces are transmitted through the interface; with the addition of FBS to the drop, the beads immediately stop moving (Movie S1). We conclude that FBS and SR (two of the most widely used additives in mammalian cell culture media) rapidly induce the formation of a no-slip boundary. We now apply this boundary condition to develop a theoretical model.

Semi-analytical model to describe fluid-walled conduits

Our initial aim is to model a straight conduit with known flow rates provided by a syringe pump (Fig. 1c). We first consider the standard solution for flow between parallel plates derived from the momentum equation (the Supplementary Information gives full derivations for this and other equations). The resultant pressure gradient is $\frac{dP}{dx} = \frac{8\mu u_{max}}{h_{max}^2}$ (μ = viscosity, u_{max} = maximum velocity). As the cross-section of fluid-walled conduits can be represented by the segment of a circle where height is expressed locally as $h_z = \sqrt{R^2 - z^2} - b$, the flow rate ($Q$) becomes ($Q = uA$; u = velocity, A = cross-sectional area):

$$Q = \frac{4}{3}\int_0^a \frac{h_z^3 u_{max}}{h_{max}^2}\, dz = \frac{4}{3}\frac{u_{max}}{h_{max}^2}\int_0^a \left(\sqrt{R^2 - z^2} - b\right)^3 dz \qquad (1)$$

The integrand is rearranged and nondimensionalized using $\eta = \frac{z}{a}$ and evaluated for the condition $a \gg h_{max}$ (defined as $\frac{h_{max}}{a} \leq 0.2$, Fig. S5), which—critically for the following solution—yields an approximately constant value for the integral, giving $Q = 0.61\, u_{max} a\, h_{max}$. Substituting this into the pressure gradient for flow between two parallel plates, we obtain $\frac{dP}{dx} = \frac{13.04\mu Q}{a\, h_{max}^3}$. For $a \gg h_{max}$, $R = \frac{a^2}{2h}$, which combined with $\Delta P_{conduit} = \frac{\gamma}{R}$ yields the semi-analytical expression for conduit height $h_{max}(x) = \left(\frac{26.08 Q\mu a x}{\gamma} + h_0^4\right)^{0.25}$ (h_0 is the maximum height at the exit, where $x = 0$). For a conduit height-to-width ratio $\frac{h_{max}}{a} =$ 0.2 (within our operational range), the associated error is ~4%, which is a result of our simplification of the radius of curvature of a conduit from $a \gg h_{max}$.

This solution enables the height at any position in a conduit to be predicted if the boundary condition h_0 is known. Evaluating the magnitude of the bracketed term $\frac{26.08 Q\mu a x}{\gamma h_0^4}$, we find that for a conduit with $a = 400$ µm, $\mu =$ 1 cP, $Q = 25$ µL/h, $\gamma = 0.04$ N/m, and $h_0 = 20$ µm (as an order of magnitude reference), the effect of the boundary condition on the height >1 mm away from the exit is small. This provides a favorable corollary; height can be predicted by the simplified power law:

$$h_{max}(x) = \left(\frac{26.08 Q\mu a x}{\gamma}\right)^{0.25} \qquad (2)$$

Hence, we do not require h_0 to be known to predict the conduit height for most experimental conditions of interest.

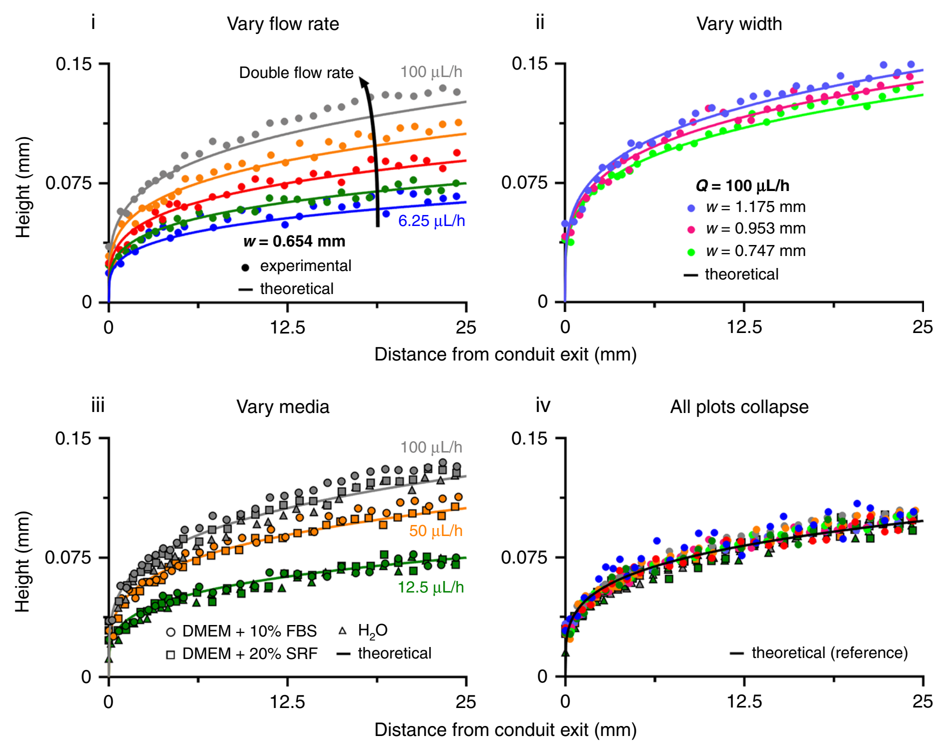

Fig. 3 Effects of varying conditions on the maximum conduit height. Individual points: h_{max} measured as in Fig. 2 over the conduit length (25 mm). Continuous lines: theoretical predictions based on Eq. 2 (in iv, using $Q = 25$ µL/h and $w = 953$ µm). (i) Varying flow rate (conduit width ~650 µm). (ii) Varying conduit width (flow rate 100 µL/h). (iii) Varying medium flowing through the conduit (width ~650 µm). Conduits are either prepared using DMEM + 10% FBS and perfused with the same medium (circular points) or H_2O (triangular points) or prepared and perfused using DMEM + 20% SR (square points). The heights at each flow rate are almost identical to those of DMEM + 10% FBS. (iv) Height measurements of all conduits collapsed onto a single reference plot according to Eq. S38 (color codes as in i and ii), demonstrating that Eq. 2 predicts the conduit heights for varying conditions.

The semi-analytical solution predicts experimentally measured heights

We next measure the heights of conduits made with DMEM + 10% FBS (from the exit to 25 mm upstream) using the approach outlined in Fig. 2 and compare the results with those predicted by Eq. 2 using $\gamma = 0.022$ N/m (obtained from pendant-drop tensiometry; see the Supplementary Information) and $\mu = 0.94$ cP (at 25 °C;[24]). In all cases, the predicted results fit the experimental data well, for example, as the flow and conduit width vary (6.25 µL/h ≤ Q ≤ 100 µL/h in Fig. 3i and ~750–1175 µm in Fig. 3ii). Good fits are also obtained with conduits printed and perfused with medium plus 20% SR and conduits printed with medium plus 10% FBS and then perfused with water (Fig. 3iii); this suggests that components in FBS and SR are deposited on the conduit walls and ceilings during conduit construction and create long-lived no-slip boundaries. Therefore, we examine the stability of the boundary with and without continuous flow for 24 h before measuring the heights (with flow). Although the variance in the height over time is small between experiments (Fig. S8), the dynamic nature of interfacial tension can be expected to introduce a time-dependent variable explaining the small differences measured. We also show that the measured heights match the predictions through mapping on a single reference plot (Fig. 3iv; Eq. S42). Finally, we compare the predictions obtained from the semi-analytical solution with those from a numerical model that does not require the h/a simplification implicit in our power law; there is excellent agreement at scales relevant to this study (Fig. S6; Supplementary Information).

Predicting the wall shear stress

The wall shear stress, $\tau_{\max}$, is evaluated at $y = \pm\frac{h}{2}$, with $\tau_{\max} = \mu\frac{\partial u}{\partial y}$ and $\frac{\partial u}{\partial y} = \frac{8yu_{\max}}{h_{\max}^2}$. We then use the relationship $u_{\max(z)} = \frac{u_{\max(0)}}{h_{\max}^2}h_z^2$ to infer $\tau_{\max(z)} = \tau_{\max(0)}\frac{h_z}{h_{\max}}$. $\tau_{\max}$ is then expressed in terms of $h_{\max}$ using Eq. 2, yielding:

$$\tau_{\max(z)} = 1.28\sqrt{\frac{\mu\gamma Q}{a^3 x}}\frac{h_z}{h_{\max}} \tag{3}$$

Chokes reduce height variations down conduits

Controlling shear stress is essential for many cell studies; this is easily achieved in solid-walled systems with fixed

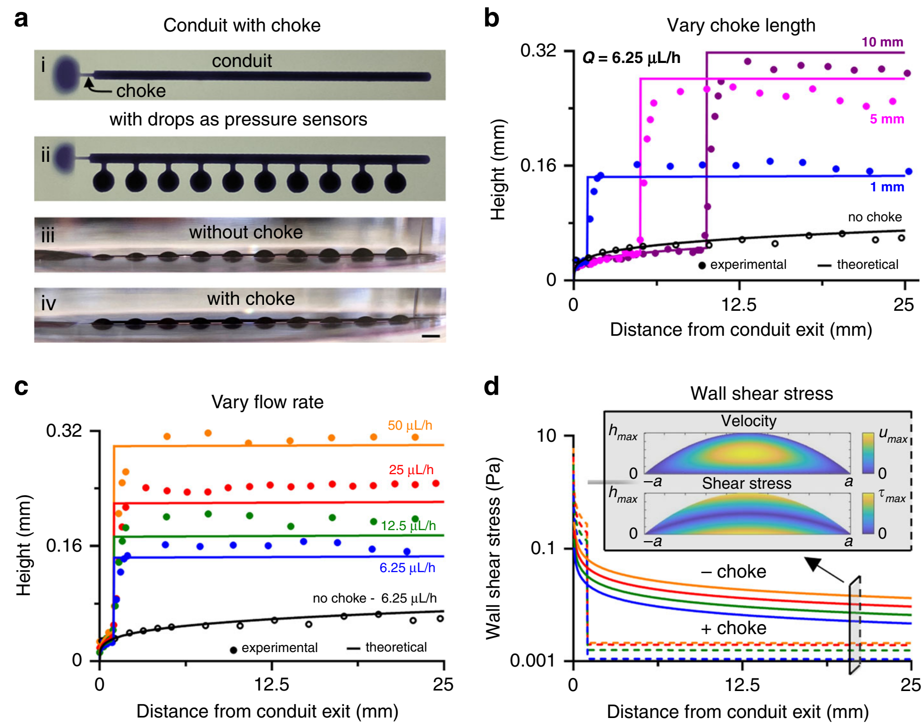

Fig. 4 Chokes suppress variations in h_{max} and shear stress along conduits. Generally, conduits (width ~950 µm) are connected to exit chokes (width ~400 µm). The lines in the graphs show the theoretical results from Eq. 2. **a** Images. Blue dye is added to aid visualization of the flow to the left. Bar: 2 mm. (i) Top view of conduit (length 24 mm) with choke (length 1 mm). (ii) Top view of a conduit + choke (as i) with attached pressure sensors/drops. (iii, iv) Side views of a conduit (length 25 mm) + sensors and conduit (length 24 mm) + sensors plus choke (1 mm). The sensor-drop height reflects the local pressure in the main conduit. Without a choke, the drop height decreases in the direction of flow with distance from the exit; with a choke, the heights (and thus the pressures) remain more uniform down the conduit. **b** Varying choke lengths (1, 5, and 10 mm; as the choke length increases, the conduit length decreases, so all structures are 25 mm long). **c** Height variations are stabilized at different levels at different flow rates (conduit length 24 mm, choke length 1 mm). **d** Shear stresses (calculated semi-analytically from Eq. 3) down conduits ± chokes (conduit length 24 mm, choke length 1 mm). The line colors represent the same conditions as those in panel (**c**). Solid lines—without choke; dashed lines—with choke. Chokes ensure that the shear stress is more uniform down the conduit. Inset: normalized velocity and shear stress profiles applied to any flow rate across the circular cross-section of any conduit ± choke (see Supplementary Information).

geometries.[12] In our conduits, the height increases from the exit as one progresses further upstream, which translates into corresponding variations in shear stress. In addition, $\frac{dh}{dx}$ progressively decreases as the distance from the exit increases (from Eq. 2, $h \propto x^{0.25}$, and so $\frac{dh}{dx} \propto x^{-0.75}$). Consequently, approximately uniform fields of wall shear stress ($\frac{d\tau}{dx}$) are only found tens of centimeters from the exit, so conduits with the relatively uniform fields required by biologists cannot be built in a 6 cm dish. Therefore, we add a short narrow conduit (a choke) to the exit of the conduit so that the choke bears most of the pressure drop and creates a field of nearly uniform shear throughout the conduit (Fig. 4ai). Due to the choke, $h_{conduit} \propto (\frac{a_{conduit}}{a_{choke}})^2$; then, the effective length (x_{eff}) introduced by the choke, at which $h = h_{conduit}$ for a conduit without a choke, is $x_{eff} = x_{choke}(\frac{a_{conduit}}{a_{choke}})^7$. From Eq. 3, $(\frac{d\tau}{dx})_{no\ choke} \propto (\frac{1}{ax})^{\frac{3}{2}}_{conduit}$, so $(\frac{d\tau}{dx})_{choke} \propto (\frac{1}{a_{conduit}x_{eff}})^{\frac{3}{2}}$. Hence, the change in $\frac{d\tau}{dx}$ from the addition of a choke is $\frac{(\frac{d\tau}{dx})_{no\ choke}}{(\frac{d\tau}{dx})_{choke}} \propto (\frac{a_{conduit}}{a_{choke}})^{\frac{21}{2}}$. Therefore, for conduits in Fig. 4b, the change in τ over 1 cm upstream of the choke is marginal (in order of increasing choke length, the values are 0.85%, 0.20%, and 0.15%), and the wall shear stress is effectively constant in the flow direction.

To illustrate the effect of a choke on the conduit height, we print a conduit with 10 connected drops (Fig. 4aii). During flow, the pressure in each drop matches the local pressure in the conduit at the connection point; therefore, each drop serves as an independent pressure sensor. Without a choke, the drop height decreases in the direction of flow as the pressure falls (Fig. 4aiii). With a choke, all sensors have approximately similar heights (Fig. 4aiv). The wall shear stresses calculated from Eq. 3 also show that choked conduits have more constant fields along their lengths that are up to 2 orders of magnitude smaller than those of choke-free conduits (Fig. 4d). The predicted velocity and shear-stress fields across the

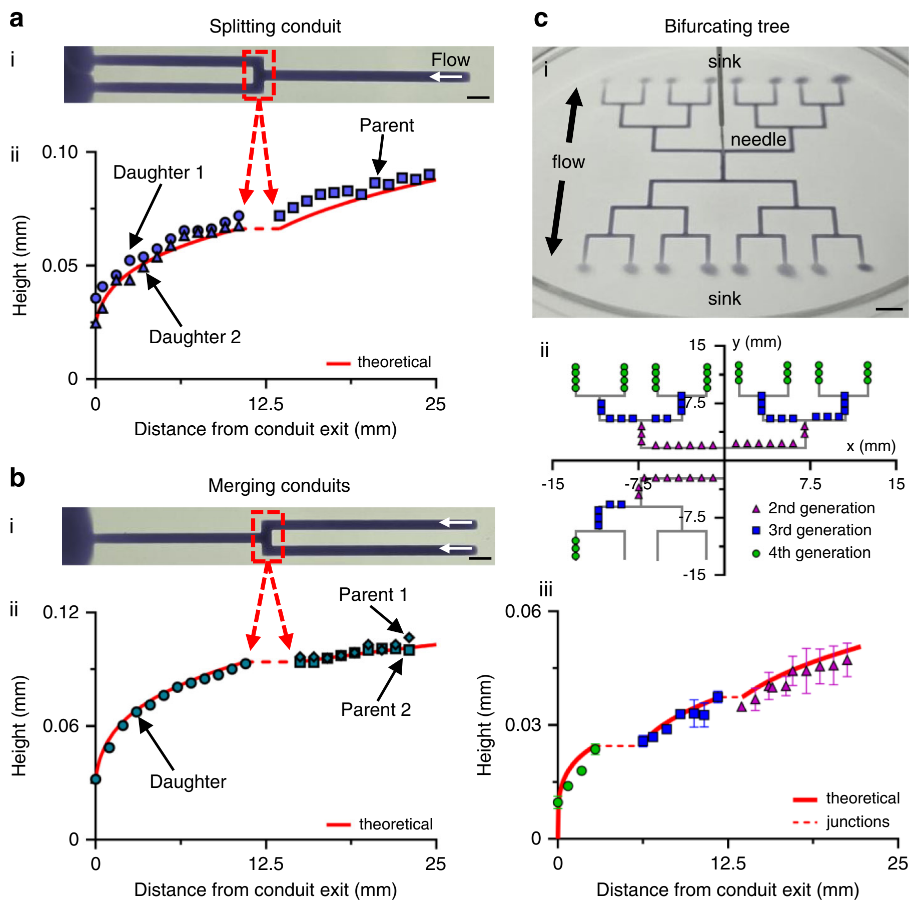

Fig. 5 Splitting, merging and bifurcating circuits. Conduit heights are measured as described in Fig. 2. Red line in plots: theoretical height predictions from Eq. 2 (dashed portions correspond to junctions and assume no local pressure drop). Bars in images: 2 mm. **a** Splitting conduit. (i) Image (conduit width ~650 µm). (ii) Heights down parent and daughters (input into parent 25 µL/h). **b** Merging conduits. (i) Image (conduit width ~650 µm). (ii) Heights down conduits (both parents perfuse at 25 µL/h). **c** Bifurcating tree. (i) Image (6 cm dish; conduit width ~550 µm). (ii) Tree plan (gray line) showing where heights are measured (colored symbols indicate the daughter generation). (iii) Plot indicating the concordance between the measured (symbols colored the same as those in cii) and predicted heights.

conduit width are shown in the inset in Fig. 4d. Strikingly, 25% of the width experiences < 5% variation in shear stress (yellow region in the inset). Human umbilical vein endothelial cells (HUVECs)—chosen because they are known to respond to shear stress—grow as expected[5] in such a choked conduit (Fig. S12).

Predicting flows in complex networks

This theory for single conduits can be extended to networks where conduits split or merge (as in vascular trees). We begin with a network in which input (parent) and output (daughter) conduits have the same width. The output flow (Q_d) is determined by continuity, so for one input (flow rate Q_p) splitting into n outputs, $Q_d = \frac{Q_p}{n}$. If instead, m inputs (with the same Q_p) merge into a single output, then $Q_d = m \times Q_p$. This process can be repeated to determine flows emerging from each node in a complex tree. The semi-analytical solution is then applied iteratively through each conduit starting from the exit.

We first study one conduit splitting into two daughters (Fig. 5a), then the same structure with reversed flow (Fig. 5b), and finally a bifurcating tree with four generations of daughters (Fig. 5c). All parents and daughters have the same widths, but the flow area at the junction increases, so the local pressure drop is small and assumed to be negligible. The theoretical predictions fit well with the experimental height measurements (Fig. 5). This theory may also be extended to networks in which conduits have different lengths and widths (Supplementary Information).

Discussion

Our challenge was to predict flow through a straight fluid-walled conduit built using a cell culture medium on a standard 6 cm Petri dish; during flow, the cross-section of such a conduit inevitably morphs above an unchanging footprint (i.e., it expands as flow increases and shrinks with distance from the input; Fig. 1c). Our approach is based on the recognition that the conduit height reflects the local pressure. Therefore, we develop a method to measure height (Fig. 2) and find that the addition of FBS or SR to the medium creates a solid medium:FC40 interface that induces no-slip boundary conditions; this defines the boundary conditions for our model (Fig. 2). Therefore, it is likely that fluids rich in albumin (e.g., that in the vasculature, lymph, cerebrospinal fluid, and vitreous humor) yield the same no-slip conditions. We next establish a simple power law with a fixed exponent (Eq. 2) by approximating the conduit cross-section and applying no-slip boundary conditions. This power law enables the prediction of the conduit height, flow field, and shear stress (Eq. 3) anywhere in a conduit; it requires no additional boundary conditions beyond the conduit footprint, flow rate, viscosity of the medium, and interfacial tension. This level of information is essentially similar to that required with laminar flow through a solid-walled pipe, except the pipe diameter now morphs in the flow direction to enable the pressure gradient induced by interfacial tension to satisfy the momentum equation. This law also agrees with numerical predictions for conduits satisfying $h/a < \sim 0.2$, which is in the practical range. This enables users to design conduits and to predict a priori flows and shear stresses matching their specific requirements, including those with essentially uniform shear-stress profiles through the addition of chokes (in the absence of chokes, such conduits would be too long to fit in a 6 cm dish). We also experimentally demonstrate the interplay between the conduit height and pressure by printing 10 drops connected at different points down a conduit; then, during flow, each drop serves as an independent pressure sensor (as the height reflects the local pressure; Fig. 4a). We also experimentally verify the accuracy of the model by varying flows through conduits with a range of widths (Fig. 3), splitting and merging conduits (Fig. 5a, b) and using a fractal vascular tree (Fig. 5c). As this form of open microfluidics offers multiple advantages over traditional closed systems[20–22] we anticipate that this model will increase the uptake of these circuits in domains benefiting from flow (e.g., when generating chemotactic gradients using laminar streams) and well-defined shear stress (e.g., when studying thromboses in vascular trees).

Materials and methods

Fluid-walled microfluidic circuit fabrication

All circuits were fabricated using a custom-made programmable printer (iotaSciences Ltd, Oxford, UK). The printer is fitted with a syringe pump that drives a 1 mL glass syringe (Hamilton, Reno, Nevada, USA). The syringe is filled with the immiscible and bioinert fluorocarbon FC40 (FC40STAR®, iotaSciences Ltd, Oxford, UK) and connected via polytetrafluoroethylene (PTFE) tubing (26 G, Adhesive Dispensing Ltd, Milton Keynes, UK) to a laser-cut jetting needle (25 G, 70 µm inner diameter, Oxford Lasers, Didcot, UK) held by the printer's 3-axis traverse system.

Circuits were made on 60 mm tissue culture-treated dishes (Corning, 430166). First, 1 mL of cell culture medium is pipetted on the dish and swirled until it covers the entire bottom of the dish. The medium is either DMEM (Merck) + 10% FBS (Merck) or DMEM + 20% SR (Thermo Fisher). The dish is then tilted so that the excess medium drains to the side, and most of the medium removed by pipetting, leaving a thin residual film (~30 µm thick) on the bottom. This film is overlaid with 2 mL FC40 (Fig. 1a), the dish is placed on the stage of the printer, and the jetting needle is lowered until the tip is 0.5 mm above the bottom of the dish. FC40 is now jetted (8 µL/s) as the needle moves laterally above the surface of the dish. As the submerged FC40 jet contacts the dish's surface, it pushes the medium aside to leave fluid walls of FC40 pinned to the dish by interfacial forces. These walls then shape the conduit.

Perfusing fluid-walled conduits

A 250 µL glass syringe (Hamilton) filled with medium and placed in a syringe pump (PhD Ultra, Harvard Apparatus) is connected via PTFE tubing to a 25 G stainless-steel hollow needle (Adhesive Dispensing Ltd). The needle is lowered through the ceiling into the conduit ~30 mm from the exit until it is ~100 µm above the bottom of the dish, and the dish is placed on the stage of an inverted microscope. The syringe pump is then started, and conduit heights are measured once the pressures in the conduits reach equilibrium, after ~30 min. The open-ended straight conduits are 25 mm long unless stated otherwise.

Measuring the conduit height

The conduits in Figs. 3 and 4 were imaged on a Zeiss Axio Observer inverted microscope with a 10X Plan Apochromat Air objective (NA = 0.3), and those in Fig. 5 and S8 were imaged on an Olympus IX53 inverted microscope with a 40X objective (NA = 0.55). The conduit heights are measured as the conduits are perfused with medium plus red fluorescent beads (1:1000 mixture; 0.5 µm diameter; FluoSpheres, F8812, Thermo Fisher). After equilibration for ~30 min after the beginning of perfusion, some beads remain stationary on the surface of the dish or the medium:FC40 interface and are used for height measurements (Fig. 2). To validate the theoretical model, we experimentally measure h_{max} and correct the heights for the apparent depth due to refraction (Eq. S40).

The Zeiss microscope has a motorized stage and a digital controller that can record coordinates to within tens of nm. It displays real-time images on a monitor, with cross-hairs indicating the exact position (Fig. 2c). Starting from the conduit exit, this digital controller is used to position the objective close to the center of the conduit, and a static bead on the medium:FC40 ceiling is brought into focus. The coordinates are recorded, and the stage is lowered to focus on a static bead on the dish surface (there are typically many). The coordinates are again recorded. The stage is then moved laterally to record the edge coordinates of the conduit. The offset z between the bead on the ceiling and the center of the conduit and the corresponding height at this point, h_z, are now calculated. $h_{\max}$ is then inferred using trigonometry, and the measurements are repeated along the length of the conduit. In the first 5 mm (where the conduit height increases most rapidly), measurements are taken every 0.5 mm, and in the remaining 20 mm steps, the measurement interval is increased to 1 mm. The stage of the Olympus microscope lacks digital control and is less precise, and the approximate location of the center of the conduit is determined using the circular nature of the fluid interface; moving the objective upwards scans through beads stuck on the interface, getting closer to the top of the conduit as the objective is raised. The top is identified when only one or a few beads remain in focus (typically in an axial strip), and this position is recorded using the scale on the objective knob of the microscope (ticks spaced in 1 µm increments). The position on the surface of the dish directly below this bead is also recorded, and the difference is $h_{\max}$. This process is then repeated along the entire conduit as before. Pictures of the conduit are then taken with a 4X objective to obtain its average width.

Due to mismatches between the refractive indices of the culture medium and air, height differences measured on microscopes using the focal position of beads do not reflect the axial movement of the microscope objective; rather, the height differences appear smaller.[26] Height corrections are dependent on the objective numerical aperture and refractive indices, which for our experiments are found to be $\Delta f = \alpha \times \Delta s$, where Δf is the actual conduit height, Δs is the measured height, and α is a constant ($\alpha = 1.36$ for Zeiss measurements; $\alpha = 1.45$ for Olympus measurements).

Acknowledgements

This work was supported by iotaSciences Ltd. (who provided financial support for C.D., F.N., and C.S.), the William H.G. FitzGerald Scholarship (N.S.-K.), the Impact Acceleration Account of the Biotechnology and Biological Sciences Research Council (P.R.C. and E.J.W.), and awards from the Medical Research Council under the Confidence in Concept scheme (MC_PC_15029 to P.R.C. and E.J.W).

Author details

[1]Department of Engineering Science, Osney Thermo-Fluids Laboratory, University of Oxford, Oxford OX2 0ES, UK. [2]Sir William Dunn School of Pathology, University of Oxford, Oxford OX1 3RE, UK. [3]Cold Spring Harbor Laboratory, Cold Spring Harbor, NY, USA

Author contributions

C.D. and N.S.-K. contributed equally. C.D., N.S-K., P.R.C., and E.J.W. designed the research; C.D., N.S-K., F.N., C.S., and E.J.W. performed experiments; C.D., N.S-K., F.N., C.S., and E.J.W. analyzed data; and all authors worked on the paper.

Conflict of interest

P.R.C. and E.J.W. each hold equity in and receive fees from iotaSciences Ltd., a company exploiting this technology; iotaSciences Ltd. also provided the printers, the FC40STAR®, and financial support for C.D., F.N., and C.S.

Supplementary information The online version contains supplementary material available at https://doi.org/10.1038/s41378-021-00322-6.

Received: 4 August 2021 Revised: 3 October 2021 Accepted: 8 October 2021
Published online: 18 November 2021

References

1. Huber, D. et al. Hydrodynamics in cell studies. *Chem. Rev.* **118**(Feb), 2042–2079 (2018).
2. Novak, R. et al. Robotic fluidic coupling and interrogation of multiple vascularized organ chips. *Nat. Biomed. Eng.* **4**, 407–420 (2020).
3. Park, S. E., Georgescu, A. & Huh, D. Organoids-on-a-chip. *Sci. (80-.).* **364**(Jun), 960 LP–960965 (2019).
4. Tuveson, D. & Clevers, H. Cancer modeling meets human organoid technology. *Sci. (80-.).* **364**(Jun), 952 LP–952955 (2019).
5. Shemesh, J. et al. Flow-induced stress on adherent cells in microfluidic devices. *Lab Chip* **15**, 4114–4127 (2015).
6. Stone, H. A., Stroock, A. D. & Ajdari, A. Engineering flows in small devices: microfluidics toward a Lab-on-a-Chip. *Annu. Rev. Fluid Mech.* **36**(Jan), 381–411 (2004).
7. Blonski, S. et al. Impact of inertia and channel angles on flow distribution in microfluidic junctions. *Microfluid. Nanofluidics* **24**, 14 (2020).
8. Raj, A., Suthanthiraraj, P. P. A. & Sen, A. K. Pressure-driven flow through PDMS-based flexible microchannels and their applications in microfluidics. *Microfluid. Nanofluidics* **22**, 128 (2018).
9. Bahrami, M., Yovanovich, M. M. & Culham, J. R. Pressure drop of fully-developed, laminar flow in microchannels of arbitrary cross-section. *J. Fluids Eng.* **128**(Jan), 1036–1044 (2006).
10. Kaliviotis, E., Sherwood, J. M. & Balabani, S. Local viscosity distribution in bifurcating microfluidic blood flows. *Phys. Fluids* **30**(Feb), 30706 (2018).
11. Lu, X., Galarneau, M. M., Higgins, J. M. & Wood, D. K. A microfluidic platform to study the effects of vascular architecture and oxygen gradients on sickle blood flow. *Microcirculation* **24**(Jul), https://doi.org/10.1111/micc.12357 (2017).
12. Zografos, K., Barber, R. W., Emerson, D. R. & Oliveira, M. S. N. A design rule for constant depth microfluidic networks for power-law fluids. *Microfluid. Nanofluidics* **19**, 737–749 (2015).
13. Marušić-Paloka, E. Fluid flow through a network of thin pipes. *Comptes Rendus l'Académie des. Sci. - Ser. IIB - Mech.* **329**, 103–108 (2001).
14. Berthier, J., Brakke, K. & Berthier, E. *Open Microfluidics*. Wiley (2016).
15. Berthier, J., Theberge, A. B. & Berthier, E. Open-channel microfluidics. *Fundamentals and applications*. Morgan & Claypool Publishers (2019) https://doi.org/10.1088/2053-2571/ab21ca.
16. Li, C. et al. Under oil open-channel microfluidics empowered by exclusive liquid repellency. *Sci. Adv.* **6**(Apr), eaay9919 (2020).
17. Towell, G. D. & Rothfeld, L. B. Hydrodynamics of rivulet flow. *AIChE J.* **12**(Sep), 972–980 (1966).
18. Qian, S., Joo, S. W., Jiang, Y. & Cheney, M. A. Free-surface problems in electrokinetic micro- and nanofluidics. *Mech. Res. Commun.* **36**, 82–91 (2009).
19. van Lengerich, H. B., Vogel, M. J. & Steen, P. H. Coarsening of capillary drops coupled by conduit networks. *Phys. Rev. E* **82**(Dec), 66312 (2010).
20. Soitu, C. et al. Jet-printing microfluidic devices on demand. *Adv. Sci.* (2020) https://doi.org/10.1002/advs.202001854.
21. Soitu, C. et al. Microfluidic chambers using fluid walls for cell biology. *Proc. Natl. Acad. Sci.* (2018) https://doi.org/10.1073/pnas.1805449115.
22. Walsh, E. J. et al. Microfluidics with fluid walls. *Nat. Commun.* **8**, 816 (2017).

23. Calver, S. N., Gaffney, E. A., Walsh, E. J., Durham, W. M. & Oliver, J. M. On the thin-film asymptotics of surface tension driven microfluidics. *J. Fluid Mech.* **901**, A6 (2020).
24. Giaever, I. & Keese, C. R. Behavior of cells at fluid interfaces. *Proc. Natl Acad. Sci. U.S.A.* **80**(Jan), 219–222 (1983).
25. Keese, C. R. & Giaever, I. Cell growth on liquid interfaces: role of surface active compounds. *Proc. Natl Acad. Sci. U.S.A.* **80**(Sep), 5622–5626 (1983).
26. Visser, T. D., Oud, J. L. & Brakenhoff, G. J. Refractive index and axial distance measurements in 3-D microscopy. *Opt. (Stuttg.)* **90**, 17–19 (1992).

Supplementary Information for

Predicting flows through microfluidic circuits with fluid walls

Cyril Deroy, Nicholas Stovall-Kurtz, Federico Nebuloni, Cristian Soitu, Peter R. Cook*, Edmond J. Walsh*

Corresponding authors:

*Peter R. Cook
Email: peter.cook@path.ox.ac.uk

*Edmond J. Walsh
Email: edmond.walsh@eng.ox.ac.uk

This Word file includes:

- Supplementary text
- Figures S1 to S12
- Tables S1 to S4
- Legend for Movie S1
- SI References

Other supplementary materials for this manuscript include the following:

- Movie S1

Supplementary Information Text

Semi-analytical solution for fluid-walled conduits

The solution to flow through fluid-walled conduits is derived from the simplified Navier-Stokes equation:

$$\rho\left(u\frac{\partial u}{\partial x}+v\frac{\partial u}{\partial y}\right)=-\frac{\partial P}{\partial x}+\mu\left(\frac{\partial^2 u}{\partial x^2}+\frac{\partial^2 u}{\partial y^2}\right) \qquad (S1)$$

Flow is laminar (the Reynolds number of our conduits never exceeds 0.1; Table S1), unidirectional ($v=0$), and fully-developed ($\frac{\partial u}{\partial x}=\frac{\partial^2 u}{\partial x^2}=0$). The simplified equation becomes:

$$\frac{\partial P}{\partial x}=\mu\,\frac{\partial^2 u}{\partial y^2} \qquad (S2)$$

From Fig. 1C, we determine these geometrical relationships:

$$a^2+b^2=R^2$$
$$R=b+h_{max}$$
$$R=\frac{a^2+h_{max}^2}{2h_{max}} \qquad b=\frac{a^2-h_{max}^2}{2h_{max}}$$

Conduit height, h_z, at any location across the half width (Fig. 2B) is:

$$h_z=\sqrt{R^2-z^2}-b \qquad (S3)$$

At the center of the conduit ($z=0$), height is maximal and corresponds to h_{max}; at pinning lines ($z=\pm a$), it is 0. The width and length of the conduit are set by the user and do not change over time. However, h_{max} depends on the pressure which changes during flow as fluid walls morph; it increases with increasing pressure, and decreases in the direction of flow. From the provided boundary conditions, the dimensionless velocity profile is assumed to be the same as that used in the classical solution of Poiseuille flow between parallel plates, and – as media:FC40 interfaces act as solid boundaries – we assume the no-slip boundary condition applies:

$$@y=\pm\frac{h_{max}}{2};u=0 \quad and \quad @y=0;\frac{du}{dy}=0$$

Integrating Eq. S2 twice yields:

$$\frac{du}{dy}=\frac{1}{\mu}\frac{dP}{dx}y+c_1, \qquad u(y)=\frac{1}{2\mu}\frac{dP}{dx}y^2+c_1y+c_2$$

Applying boundary conditions, we find:

$$c_1 = 0; \quad c_2 = -\frac{1}{8\mu}\frac{dP}{dx}h_{max}^2$$

And so $u(y)$ can be expressed as:

$$u(y) = \frac{1}{2\mu}\frac{dP}{dx}\left(y^2 - \frac{h_{max}^2}{4}\right) \qquad (S4)$$

Since $u(y) = u_{max}$ @ $y = 0$, the flow's maximum velocity becomes:

$$u_{max} = -\frac{h_{max}^2}{8\mu}\frac{dP}{dx} \qquad (S5)$$

$$\therefore u(y) = \left(1 - \frac{4y^2}{h_{max}^2}\right)u_{max}, \qquad \frac{dP}{dx} \propto \frac{u_{max}}{h_{max}^2}$$

Across the conduit's width (in the z-direction), $\frac{dP}{dx}$ = constant; hence, the relationship between the maximum flow velocity across a width, $u_{max\,(z)}$, to the maximum conduit velocity, $u_{max\,(0)}$, is:

$$\frac{u_{max(0)}}{h_{max}^2} = \frac{u_{max(z)}}{h_z^2}$$

$$u_{max(z)} = \frac{u_{max(0)}}{h_{max}^2}h_z^2 \qquad (S6)$$

The total flow rate through the conduit is found by integrating the velocity profile:

$$Q = \int_{-a}^{a}\int_{-\frac{h_z}{2}}^{\frac{h_z}{2}} u(y)dydz$$

Evaluating the first integral provides flow rate per unit length as:

$$Q' = \int_{-\frac{h_z}{2}}^{\frac{h_z}{2}} u(y)dy = -\frac{h_z^3}{12\mu}\frac{dP}{dx} = \frac{2}{3}u_{max(z)}h_z$$

$$\therefore Q = \int_{-a}^{a} \frac{2}{3} u_{max(z)} h_z dz \qquad (S7)$$

Substituting for u_z in Eq. S7 as in Eq. S6 yields:

$$Q = \frac{2}{3} \frac{u_{max(0)}}{h_{max}^2} \int_{-a}^{a} h_z^3 dz$$

And since from geometry $h_z = \sqrt{R^2 - z^2} - b$:

$$\therefore Q = \frac{4}{3} \frac{u_{max(0)}}{h_{max}^2} \int_{0}^{a} \left(\sqrt{R^2 - z^2} - b\right)^3 dz \qquad (S8)$$

The integrand is then normalized using $\eta = \frac{z}{a}$ and evaluated over $\frac{a}{h_{max}}$:

$$Q = \frac{4}{3} h_{max} u_{max(0)} a \int_{0}^{1} \frac{\left(\sqrt{R^2 - \eta^2 a^2} - b\right)^3}{h_{max}^3} d\eta \qquad (S9)$$

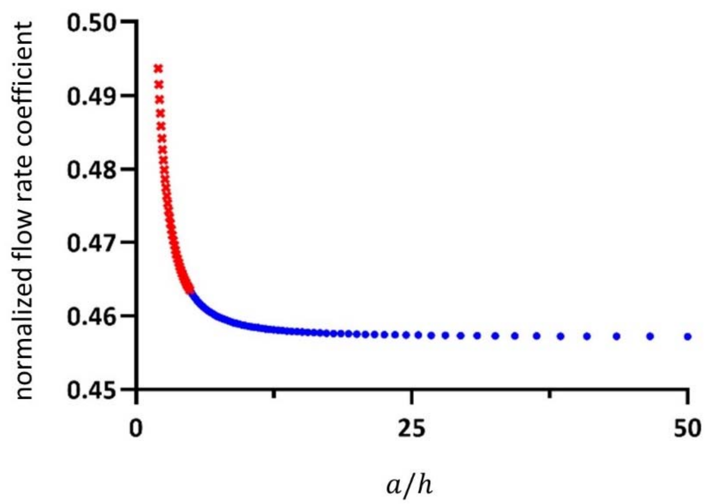

Fig. S1. Normalized volumetric flow rate coefficients for a range of conduit half width-to-height ratios. The integrand in Eq. S9 is evaluated for $0 < a/h \leq 50$. Ratios less than 5 (red crosses, $a{\sim}h$) are ignored. Ratios greater than 5 (blue dots, $a \gg h$) correspond to conduit geometries typically observed in this study. The average normalized flow rate coefficient in this region corresponds to 0.46.

For heights typically observed here ($a \gg h_{max}$; Fig S1), flow rate is:

$$Q = \frac{4}{3} h_{max} u_{max(0)} a(0.46)$$

$$\therefore u_{max(0)} = \frac{Q}{0.61 h_{max} a} \quad (S10)$$

Now substituting the relationship for $u_{max(0)}$ into Eq. S5 yields:

$$h_{max}^3 \frac{dP}{dx} = \frac{13.11 Q\mu}{a} \quad (S11)$$

The radius of curvature of the conduit is defined as $R = \frac{a^2 + h_{max}^2}{2h_{max}}$, however when $a \gg h_{max}$ the radius of curvature can be simplified as:

$$R = \frac{a^2}{2h_{max}} \left(1 + \frac{h_{max}^2}{a^2}\right) \approx \frac{a^2}{2h_{max}} \quad (S12)$$

Since change in hydrostatic pressure is assumed to be negligible along the conduit, the local pressure at any x-location can be characterized by the local Laplace pressure in accordance with the simplified Young-Laplace equation for interfaces represented as the arc of a circle ($\Delta P_{conduit} = \frac{\gamma}{R}$). Using the simplified cross-sectional radii of curvature expressed in Eq. S12 produces the following equation defining pressure increase across the interface:

$$\Delta P_{interface} = \frac{\gamma}{R} \approx \gamma \left(\frac{2h_{max}}{a^2}\right)$$

$$\therefore \frac{dP}{dx} = \frac{2\gamma}{a^2} \frac{dh}{dx} \quad (S13)$$

Substituting Eq. S13 into Eq. S11:

$$\frac{2\gamma}{a^2} h_{max}^3 dh = \frac{13.11 Q\mu}{a} dx \quad (S14)$$

$$\therefore h_{max}^3 dh = \frac{6.55 Q\mu a}{\gamma} dx \quad (S15)$$

Integrating Eq. S15 then gives:

$$h_{max}^4 = \frac{26.08 Q\mu a x}{\gamma} + c_1 \quad (S16)$$

Since at the exit, $h_{max} = h_0$, then $c_1 = h_0^4$. Hence the semi-analytical solution for predicting conduit center-heights becomes:

$$h_{max}(x) = \left(\frac{26.08Q\mu a x}{\gamma} + h_0^4\right)^{0.25} \qquad (S17)$$

Reintroducing $P \approx \gamma\left(\frac{2h_{max}}{a^2}\right)$ into Eq. S17 solves for pressure as:

$$P_x = \left(\frac{417.28Q\mu\gamma^3 x}{a^7} + P_0^4\right)^{0.25} \qquad (S18)$$

Importance of conduit exit-height

Eq. S17 requires an experimental measurement, conduit exit-height, h_0, to predict the height elsewhere in the conduit. However, consider the relative magnitude of the terms:

$$\frac{26.08Q\mu a x}{\gamma}, \qquad h_0^4$$

When $\frac{26.08Q\mu a x}{\gamma} \gg h_0^4$, exit height has a negligible effect on conduit height upstream. For given fluids, flow rate, and conduit width, the location along the conduit at which these two terms become equivalent is:

$$x = \frac{h_0^4\gamma}{26.08Q\mu a} \qquad (S19)$$

For average flow rates and conduit widths used here ($Q = 25$ µL/h, $a = 0.5$ mm), $x \approx 92$ µm. At a conservative distance from the exit (i.e., an order of magnitude greater than x; 1 mm) height predictions converge across a range of exit heights (Fig. S2). Hence, a simplified semi-analytical solution requiring no experimental measurements can predict conduit height accurately away from the exit:

$$h_{max}(x) = \left(\frac{26.08Q\mu a x}{\gamma}\right)^{0.25} \qquad (S20)$$

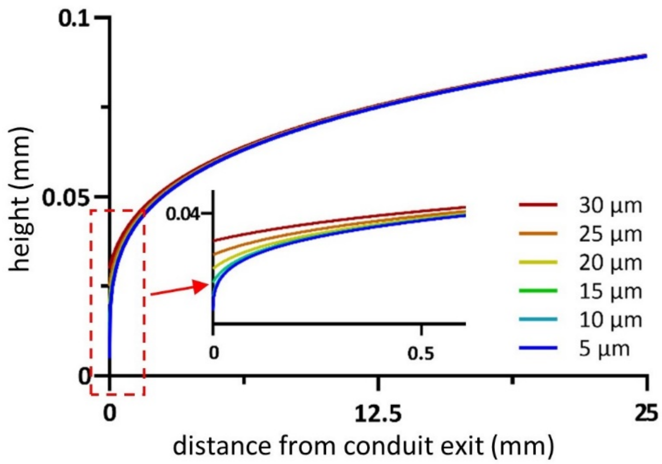

Fig. S2. The effect of exit height on conduit height is negligible. Conduit height (h_{max}) is calculated using Eq. S17 assuming exit heights (h_0) of 5 – 30 µm ($Q = 25$ µL/h, $a = 0.5$ mm). Inset: results for the first 0.6 mm. For low exit heights ($5 < h_0 < 20$), conduit heights differ markedly only in the first ~0.1 mm before converging; for larger exit heights ($h_0 = 25$ or 30 µm) convergence occurs later.

Numerical solution

The semi-analytical solution provides a simple powerful method to determine flows. However, it relies on geometrical assumptions (i.e., when deriving the normalized volumetric flow rate constant of Eq. S10, and $R = \frac{a^2}{2h}$). Therefore, we derived a numerical solution without these simplifications using the forward Euler method. Pressure along a conduit is solved iteratively in steps of Δx as:

$$P'(x) = \frac{P(x + \Delta x) - P(x)}{\Delta x}$$

$$\therefore P(x + \Delta x) = P(x) + \Delta x P'(x) \qquad (S21)$$

From Eq. S8, volumetric flow rate is defined as:

$$Q = \frac{4}{3}\frac{u_{max}(x)}{h_{max}^2(x)}\int_0^a \left(\sqrt{R^2 - z^2} - b\right)^3 dz \qquad (S22)$$

The integrand in Eq. S22 is a positive constant dependent only on local cross-section, represented by β:

$$Q = \frac{4}{3}\frac{u_{max}(x)}{h_{max}^2(x)}\beta(x) \qquad (S23)$$

Rearranging for u_{max}:

$$u_{max}(x) = \frac{3}{4}\frac{h_{max}^2(x)}{\beta(x)}Q \qquad (S24)$$

Given the initial value problem $P'(x) = \frac{8\mu u_{max}}{h_{max}^2}$ (Eq. S5), $P'(0) = \frac{8\mu u_0}{h_0^2}$, and $P(0) = \frac{\gamma}{R} = \frac{2\gamma h_0}{a^2+h_0^2}$, Eq. S21 becomes:

$$P(\Delta x) = P(0) + \Delta x P'(0) \qquad (S25)$$

$$P(\Delta x) = \frac{2\gamma h_0}{a^2 + h_0^2} + \frac{8\mu u_0}{h_0^2}\Delta x \qquad (S26)$$

From Eq. S24, $u_0 = \frac{3}{4}\frac{h_0^2}{\beta(0)}Q$, hence:

$$P(\Delta x) = \frac{2\gamma h_0}{a^2 + h_0^2} + \frac{6\mu Q}{\beta(0)}\Delta x \qquad (S27)$$

Rearranging the Young-Laplace equation yields the radius of curvature at Δx:

$$R(\Delta x) = \frac{\gamma}{P(\Delta x)} \qquad (S28)$$

This iteration is repeated for n steps ($n = \{1, \ldots, L/\Delta x - 1\}$) along any conduit of length L, and is valid for as long as the half-width is greater than or equal to the local maximum height ($a > h_{max}$). If this height exceeds the half-width, the numerical solution fails (i.e., the conduit has a contact angle > 90°). It follows that:

$$R(n+1) = \frac{\gamma}{P(n+1)} \qquad (S29)$$

$$P(n+1) = P(n) + \frac{6\mu Q}{\beta(n)}\Delta x \qquad (S30)$$

$$P(n+1) = \frac{2\gamma h_{max}(n)}{a^2 + h_{max}^2(n)} + \frac{6\mu Q}{\beta(n)}\Delta x \qquad (S31)$$

Across geometries where $a \gg h_{max}$, there is good agreement between semi-analytical and numerical solutions (see later in Fig. S5).

Pendant-drop tensiometry

To determine the interfacial tension (IFT) between the various media used in this study and FC40, we used the First Ten Angstrom 1000B Manual Drop Shape Analyzer (Model B 23A 110) plus a Point Grey Firefly MV USB camera to record drops of FC40 formed in a cuvette of medium and infer the IFT through image analysis. To do so, a 34G needle (Adhesive Dispensing Ltd) is connected to a 50 µL glass syringe (Hamilton) via PTFE tubing. The syringe is filled with FC40 and loaded onto a syringe pump (Harvard Apparatus). The needle is then lowered inside a cuvette filled with medium. A drop of FC40 is then set by infusing a desired volume through the needle. A picture of the formed drop is taken, and the software determines the IFT. Drops were imaged for 5 h, and the IFT obtained by averaging values recorded 2.5 – 5 h after starting imaging, and then averaged again over the number of repeats (3 for each medium; Fig. S3). The values obtained are $\gamma_{FBS} = 22.8 \pm 0.44$ mN/m (DMEM + 10% FBS), $\gamma_{SR} = 22.2 \pm 0.99$ mN/m (DMEM + 20% SR), and $\gamma_{beads} = 20.7 \pm 0.58$ mN/m (DMEM + 10% FBS + beads). The system was also calibrated with water (a drop of water in a cuvette of FC40), yielding $\gamma_{H_20} = 51.8 \pm 0.74$ mN/m, which agrees with values accepted in the literature.

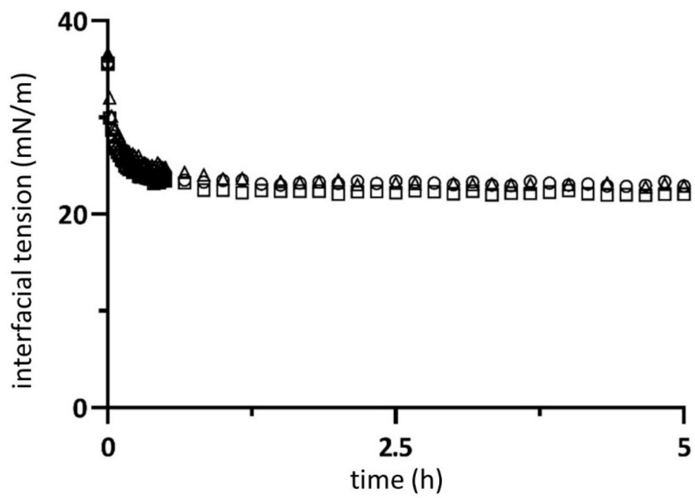

Fig. S3. Interfacial tension measurements between FC40 and DMEM + 10% FBS. Drops of FC40 were submerged in DMEM + 10% FBS, and the IFT measured over 5 h. Results of three repeats are shown, with each symbol corresponding to a repeat. In each repeat, IFT falls in the first 30 min to a plateau; the average value (γ_{FBS}) collected between 2.5 – 5 h was 22.8 ± 0.44 mN/m.

Reynolds number in fluid-walled conduits

Flow through conduits can be characterized by the Reynolds number, Re:

$$Re = \frac{\rho u_{avg} d_h}{\mu} \qquad (S32)$$

where d_h is the hydraulic diameter (often used as the characteristic length for flow through non-circular ducts or pipes in lieu of the traditional circular diameter). A duct's hydraulic diameter is:

$$d_h = \frac{4A}{P}$$

where A is cross sectional area and P is wetted perimeter. For fluidic conduits in this study, the hydraulic diameter is:

$$d_h = \frac{2\left(R^2 \sin^{-1}\left(\frac{a}{R}\right) - ab\right)}{R \sin^{-1}\left(\frac{a}{R}\right) + a}$$

Table S1 gives Reynolds numbers calculated with Eq. S32 using experimental data from Fig. 3i.

Table S1. Reynolds number in fluid-walled conduits

flow rate [µL/h]	**distance from conduit exit** [mm]	$\boldsymbol{A}$ [mm^2]	$\boldsymbol{d_h}$ [µm]	$\boldsymbol{u_{avg}}$ [mm/s]	$\boldsymbol{Re}$
6.25	0	0.0079	23.990	0.2216	0.0056
	25	0.0295	88.846	0.0591	0.0056
12.5	0	0.0100	30.647	0.3457	0.0112
	25	0.0321	96.706	0.1080	0.0111
25	0	0.0109	33.307	0.6360	0.0225
	25	0.0412	122.726	0.1685	0.0219
50	0	0.0127	38.626	1.0976	0.0450
	25	0.0518	152.258	0.2682	0.0433
100	0	0.0153	46.596	1.8162	0.0898
	25	0.0618	178.807	0.4496	0.0853

Conduit capillary length

Throughout this study, it is assumed that gravity has a negligible effect on conduit geometry as interfacial forces dominate at the microscale. The Bond number (Bo), a dimensionless quantity representing the ratio of gravitational to interfacial forces acting on a fluidic system, gives the relative importance of these forces:

$$Bo = \frac{\Delta\rho g L^2}{\gamma} \qquad (S33)$$

Here, $\Delta\rho$ denotes the difference in density between medium in the conduit and the overlaying FC40, and L some characteristic length. A system's capillary length L_c corresponds to the characteristic length at which $Bo = 1$ indicating that gravitational forces begin to dominate. For conduits in this study, $L_c = 1.6$ mm. Therefore, to neglect gravity, the characteristic length must be much less than the capillary length (i.e., $L \ll L_c$). This can be determined by investigating the Bond number, which can be written as the ratio of hydrostatic to Laplace pressures:

$$Bo = \frac{\Delta\rho g h_{max}}{\frac{\gamma}{R}} \qquad (S34)$$

Using the assumption that $a \gg h_{max}$, the radius of curvature is simplified as $R = \frac{a^2}{2h_{max}}$ yielding:

$$Bo = \frac{\Delta\rho g a^2}{\gamma} \qquad (S35)$$

Comparing this to Eq. S33, it is easy to see the characteristic length is $L = a$. As the largest half-width in this study is $a{\sim}0.6$ mm (Fig. 3ii; 2.5 times smaller than L_c), this corresponds to $Bo{\sim}0.1$, showing that interfacial forces dominate and that gravity forces are negligible.

Semi-analytical solution for perfect slip at the media:FC40 interface

The semi-analytical solution is derived with the assumption of no-slip at the media:FC40 interface. This is analogous to assuming that the ratio of the viscosities of FC40 and medium is infinite such that $\lim_{\mu_{FC40}\to\infty} \frac{\mu_{FC40}}{\mu_{media}} = \infty$. To predict flow fields in conduits with any possible ratio of dynamic viscosities, we consider the other extreme in which perfect slip exists, in absence of any Marangoni effect, between immiscible fluids such that $\lim_{\mu_{FC40}\to 0} \frac{\mu_{FC40}}{\mu_{media}} = 0$.

The steps to derive the semi-analytical solution in such conditions mirror those outlined for the no-slip condition, and vary only by the boundary conditions applied. These are:

$$@y = \frac{h_{max}}{2};\ \frac{du}{dy} = 0 \quad and \quad @y = -\frac{h_{max}}{2};\ u = 0$$

Applying these conditions to the Navier-Stokes Eq. S2 yields:

$$h_{max}(x) = \left(\frac{6.5Q\mu a x}{\gamma} + h_0^4\right)^{0.25} \qquad (S36)$$

Slip and no-slip solutions are compared in Fig. S4.

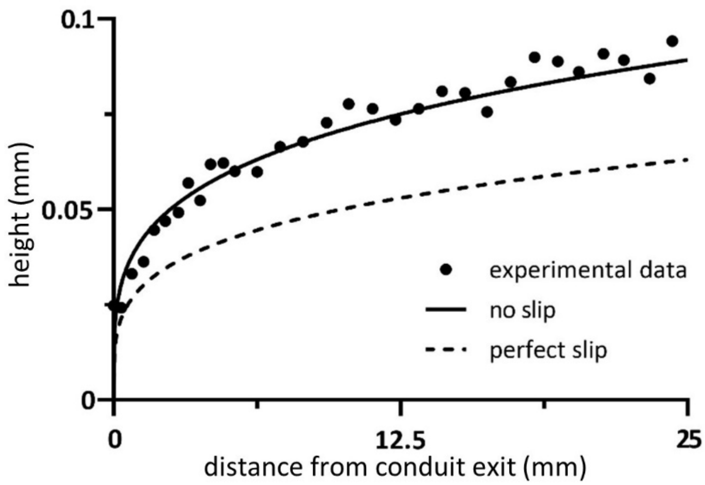

Fig. S4. Perfect slip versus no-slip semi-analytical solutions. Solutions are computed using Eq. S20 (no-slip) and Eq. S36 (slip; exit height assumed negligible) for a conduit (width 654 µm) perfused at 25 µL/h. Experimental data (reproduced from Fig. 3i) fit the no-slip condition.

Conduit failure

Conduits can withstand up to a maximum flow rate (Q_{max}) before reaching capillary instability which occurs when the contact angle exceeds 90° (defined as $\theta = \sin^{-1}\left(\frac{2ah_{max}}{a^2+h_{max}^2}\right)$). This instability occurs when half-width equals maximum height ($a = h_{max}$), producing a perfect half-circular cross-section (Fig. S5).

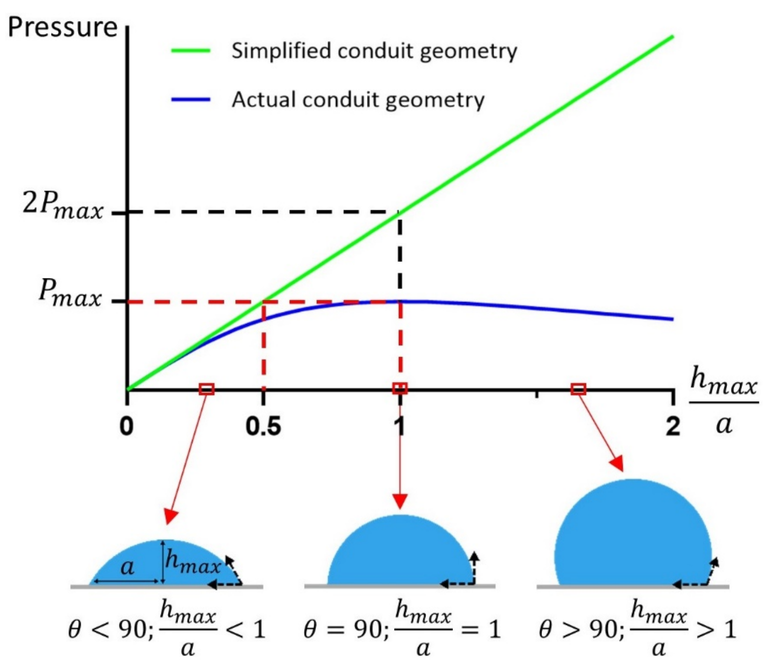

Fig. S5. Comparing pressures calculated using the simplified (green line) and exact numerical solutions (blue curve). For conduits with $\frac{h_{max}}{a} < 0.2$, the percent error between solutions is $\leq 4\%$, and – as $a \gg h_{max}$ – flow can be modelled as Poiseuille flow between two infinite parallel plates. As

$\frac{h_{max}}{a}$ increases, this simplification becomes invalid and the two solutions deviate. The maximum pressure is reached when $\frac{h_{max}}{a} = 1$; thereafter, pressure decreases as $\frac{h_{max}}{a}$ increases above unity.

Flow through conduits relies on a negative pressure gradient in the direction of flow. The maximum pressure a conduit can withstand occurs when the contact angle reaches $\theta = 90°$; beyond this point, flow further upstream begins to pool creating a bulging conduit where $\theta > 90°$. This then leads to pinning-line failure (and the fluid wall breaks). The maximum flow rates achievable in conduits will depend on circuit geometry (i.e., conduit length and width) and fluids used. Conduit failure will occur at the point of highest pressure in a straight conduit, and this will always be the inlet to the conduit. From the exact numerical model (blue curve in Fig. S5), we see that the maximum pressure is reached when $h_{max} = a$, and that this value can be extrapolated onto the simplified semi-analytical solution (Eq. S20, green curve in Fig. S5) when $h_{max} = 0.5a$. This h/a ratio is the limit at which the maximum flow rate is determined using the semi-analytical solution:

$$Q_{max} = \frac{\gamma}{26.08\mu a x} h_{max}^4$$

$$\therefore Q_{max} = \frac{\gamma a^3}{417.28\mu x} \tag{S37}$$

Fig. S5 highlights $\frac{h_{max}}{a}$ ratios where the simplified semi-analytical solution can be reliably used, which corresponds to $\frac{h_{max}}{a} \leq 0.2$, at which point there is $\leq 4\%$ error between semi-analytical and numerical solutions.

Collapsing numerical and semi-analytical solutions

There is good agreement between numerical and semi-analytical predictions of conduit properties for geometries investigated here. These theoretical projections can be collapsed onto a reference curve $h_{max,ref}$ by raising Q, a and μ to the 0.25 power and γ to the -0.25 power (see Equation S20) such as:

$$\frac{h_{max}}{h_{max,ref}} = \left(\frac{Q}{Q_{ref}}\right)^{0.25} \left(\frac{a}{a_{ref}}\right)^{0.25} \left(\frac{\mu}{\mu_{ref}}\right)^{0.25} \left(\frac{\gamma}{\gamma_{ref}}\right)^{-0.25} \tag{S38}$$

This equation accurately predicts the height profile of a conduit for any given volumetric flow rate, width, dynamic viscosity, and interfacial tension.

As our model is simplified by certain assumptions, we looked at their effect on predictions by comparing the semi-analytical model with the numerical model of the conduit (Fig. S6). Both models agree well with each other for conduit lengths of up to 100 mm, after which they diverge, differing by 6.5% at 300 mm. However, our conduits are typically ≤ 25 mm as they are printed on 6 cm dishes, so divergence is tiny.

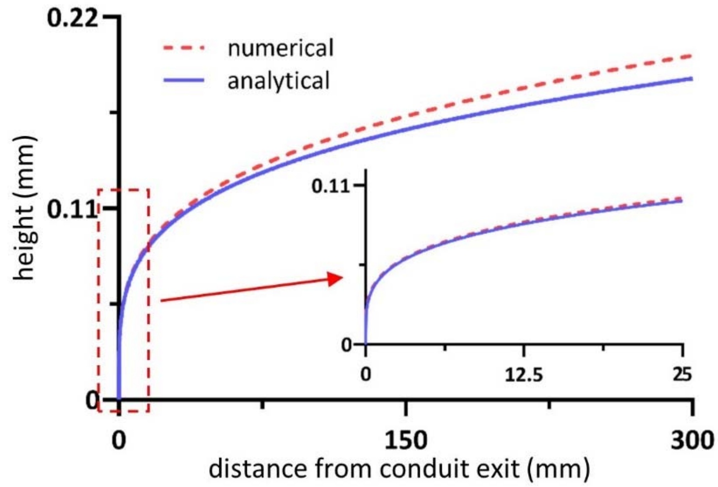

Fig. S6. Divergence of numerical and semi-analytical solutions. Heights were calculated using the iterative approach detailed in Eq. S21-31 (numerical solution), or Eq. S20 (semi-analytical solution), for a conduit with width 1 mm and flow rate 25 µL/h. Models diverge as conduit length increases, with a difference of 6.5% in conduit height 300 mm from the exit. For conduit lengths ≤25 mm relevant here (inset), the two models yield essentially similar results.

Error analysis for conduit-height predictions

To determine whether height measurements agree with theoretical predictions within an acceptable margin of error, the Root Sum of the Squares (RSS) error propagation method was used to calculate associated measurement uncertainty:

$$\varepsilon_{calc} = \sqrt{\left(\frac{\partial h_{max}}{\partial Q}\sigma_Q\right)^2 + \left(\frac{\partial h_{max}}{\partial \mu}\sigma_\mu\right)^2 + \left(\frac{\partial h_{max}}{\partial a}\sigma_a\right)^2 + \left(\frac{\partial h_{max}}{\partial x}\sigma_x\right)^2 + \left(\frac{\partial h_{max}}{\partial \gamma}\sigma_\gamma\right)^2}$$

Using u-substitution, the partial derivatives above (also known as sensitivity factors) are computed as follows:

$$\frac{\partial h_{max}}{\partial Q} = \frac{26.08\mu a x}{4\gamma\left(\frac{26.08Q\mu a x}{\gamma}\right)^{0.75}}$$

$$\frac{\partial h_{max}}{\partial \mu} = \frac{26.08Q a x}{4\gamma\left(\frac{26.08Q\mu a x}{\gamma}\right)^{0.75}}$$

$$\frac{\partial h_{max}}{\partial a} = \frac{26.08Q\mu x}{4\gamma\left(\frac{26.08Q\mu ax}{\gamma}\right)^{0.75}}$$

$$\frac{\partial h_{max}}{\partial x} = \frac{26.08Q\mu a}{4\gamma\left(\frac{26.08Q\mu ax}{\gamma}\right)^{0.75}}$$

$$\frac{\partial h_{max}}{\partial \gamma} = \frac{26.08Q\mu ax}{4\gamma^2\left(\frac{26.08Q\mu ax}{\gamma}\right)^{0.75}}$$

Next, the uncertainty of each individual variable (σ) is determined:

- σ_Q is the transducer uncertainty of the Harvard PhD Ultra syringe pump and from the user manual the pump's flow rate accuracy is $\pm 0.25\%$ ($\sigma_q = 0.0025Q$ µL/h).
- σ_μ is the standard deviation of dynamic viscosities taken from 10 separate solutions of DMEM + 10% FBS measured with a Hydramotion Viscolite 700 portable viscometer ($\sigma_\mu = 0.05$ mPa.s).
- σ_a is the standard deviation of conduit half-width along its 25 mm length (i.e., the error associated with jetting). For measurements performed on the Zeiss Axio Observer microscope, widths were measured at 35 distinct locations ($\sigma_a = 8$ µm).
- σ_x is determined by the microscope's specifications; for the Zeiss Axio Observer microscope, the accuracy of the stage in the x, y-plane corresponds to ± 1 µm ($\sigma_x = 1$ µm).
- σ_γ is unknown as interfacial tension is determined by fitting the semi-analytical solution to experimental data, and thus error in interfacial tension is not included.

Finally, error due to experimental uncertainty from the measurement of conduit height using beads (ε_{bead}) must also be included. This uncertainty takes into account the acquisition error (σ_{bead}) and twice bead diameter ($2d_{bead}$):

$$\varepsilon_{bead} = \sqrt{\sigma_{bead}^2 + 2d_{bead}^2}$$

To measure acquisition error, the distance between a single pair of beads (one on the surface of the dish and one on the media:FC40 interface) was measured 15 times and a standard deviation was calculated such that $\sigma_{bead} = 0.9$ µm. Unlike the calculated expanded sensitivity ε_{calc} which depends on location (i.e., the expected error increases as distance from the exit increases), ε_{bead} is a fixed quantity applied along the entire conduit such that the total propagated error is:

$$\varepsilon_{total} = \sqrt{\varepsilon_{calc}^2 + \varepsilon_{bead}^2}$$

Values for ε_{total} associated with height predictions are given in Fig. S7.

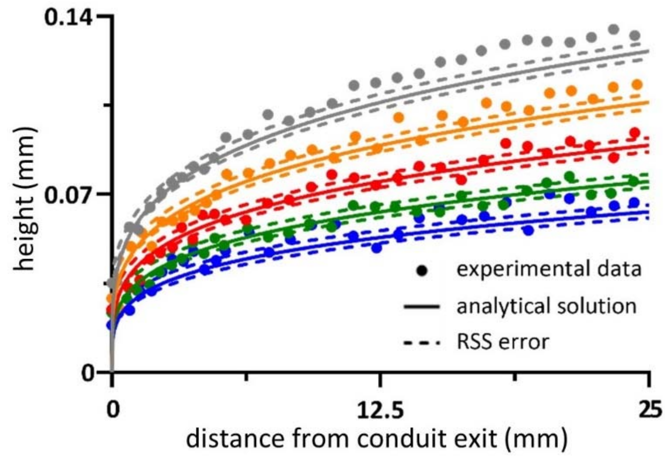

Fig. S7. Error (root sum of squares, RSS) propagation for semi-analytical predictions of conduit heights. Height predictions were calculated for conduits illustrated in Figure 3i (using Eq. S20) and errors (ε_{total}) determined (dashed lines bordering each coloured line – colour coding as in Fig. 3i).

Varying flow regimes

We studied the effect of flow regime on conduit height. First, we left a conduit at rest (no flow) for 24 h and took measurements the next day after starting flow. We then perfused a conduit overnight (for 24 h) and measured heights the following day. Comparing results with those obtained with freshly-printed conduits (Fig. 3i), although the variance of height over time is small between experiments (Fig. S8), the dynamic nature of interfacial tension could be expected to introduce a time-dependent variable to explain the small differences measured.

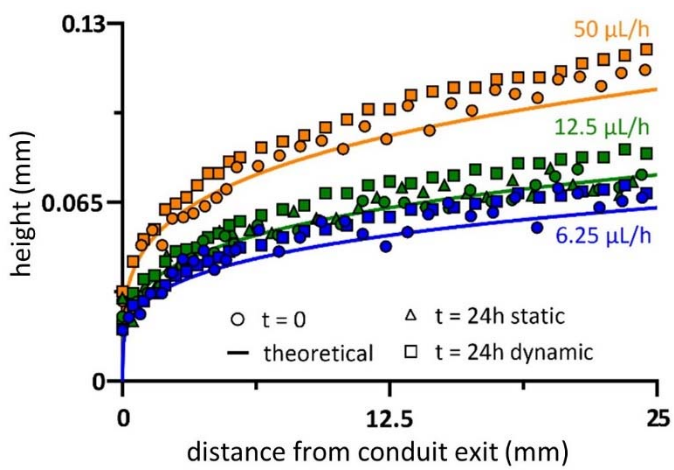

Fig. S8. Properties of fluid walls remain stable across different flow regimes. Heights in conduits experiencing different regimes were measured and compared with theoretical predictions (using Eq. 2). A conduit (width ~650 µm) was printed, left for 24 h without flow, then perfused at 12.5 µL/h, and heights measured ('t = 24 h static'). Another conduit was printed and infused for 24 h at 12.5

µL/h before measuring heights ('t = 24h dynamic'). Heights were also measured after decreasing flow to 6.25 µL/h, and then increasing it to 50 µL/h. Comparing these data with those in Fig. 3i ('t = 0') we find the different regimes had little effect on height.

Splitting conduits

In Fig. 5, we looked at the effect of one parent conduit splitting into two identical daughter conduits, and determined from continuity that flow through daughters is half the initial flow through the parent. This holds true generally for parents that split into n daughters so long as the geometry of daughters is identical. Then, $Q_d = \frac{Q_p}{n}$.

However, it is more difficult to predict flows through daughters of differing geometries. Consider Fig. S9 where some branches have different half widths a or length x.

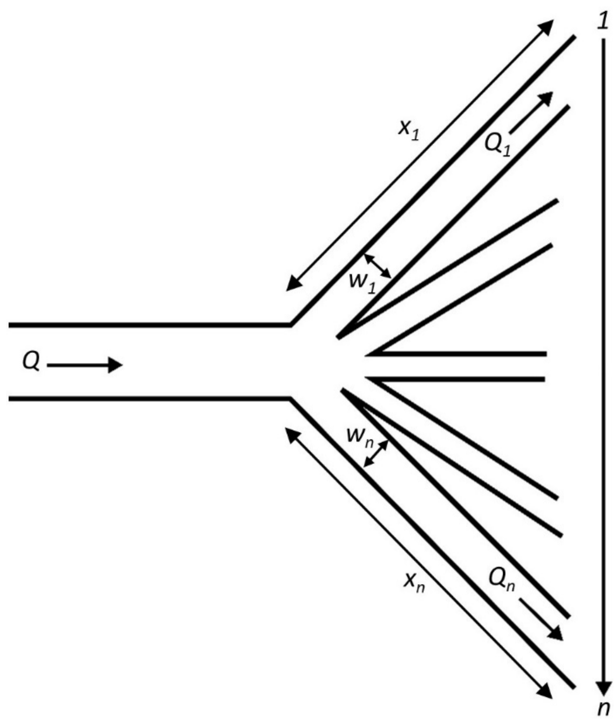

Fig. S9. Single parent conduit splitting into multiple daughter conduits. Each daughter conduit has a different length x or width w (half-width $a = \frac{w}{2}$), and therefore the resultant flow rate Q through each conduit will be different and determined by Eq. S39.

As the pressure P_{in} at the branch point must be the same for each branch, and since conduits are open ended (such that $P_0 = 0$), then $P_{in} - P_0 = \Delta P$ must be the same across each branch. From our scale analysis of the effect of exit height (h_0) on conduit shape, we know h_0 can be ignored if conduits are > 1 mm in length such that:

$$P_x = \left(\frac{417.28\gamma^3\mu Q x}{a^7}\right)^{0.25}$$

Assuming each branching conduit is > 1 mm, the pressure drop in each must be the same, and we can equate the pressure gradient in any branch n to reference branch 1 as $P_n = P_1$:

$$\left(\frac{417.4\gamma^3\mu Q_n x_n}{{a_n}^7}\right)^{0.25} = \left(\frac{417.4\gamma^3\mu Q_1 x_1}{{a_1}^7}\right)^{0.25}$$

$$\frac{Q_n x_n}{{a_n}^7} = \frac{Q_1 x_1}{{a_1}^7}$$

$$Q_n = \frac{Q_1 {a_n}^7 x_1}{{a_1}^7 x_n}$$

Applying mass conservation, we know the input flow rate Q must equal the sum of all flow through branches (from 1 to n):

$$Q = \sum_1^n Q_n = \sum_1^n \frac{Q_1 {a_n}^7 x_1}{{a_1}^7 x_n}$$

We can remove Q_1 , x_1, and a_1 from the summation term as these are used as reference values for all other channels and are fixed:

$$Q = \frac{nQ_1 x_1}{n{a_1}^7}\sum_1^n \frac{{a_n}^7}{x_n} = \frac{Q_1 x_1}{{a_1}^7}\sum_1^n \frac{{a_n}^7}{x_n}$$

This gives:

$$Q_1 = \frac{Q{a_1}^7}{x_1 \sum_1^n \frac{{a_n}^7}{x_n}} \qquad (S39)$$

Since the reference conduit can be any of the daughter conduits, we can apply this equation to calculate flow fields through any conduit knowing only input flow rate Q and the geometrical properties of each conduit.

Height correction for apparent depth in microscope measurements

To determine conduit height using an inverted microscope, we first focus on a fluorescent bead at the media-FC40 interface. The height is then taken as the distance

Δs by which the stage moves to focus on a bead on the surface of the dish. However, due to mismatches between the refractive indices of the medium containing the bead (water), and the medium surrounding the microscope objective (air), the focal position of the bead does not follow the axial movement of the stage. Rather, Δs appears smaller than reality.

To correct for this focal shift, consider Fig. S10 where the microscope stage is moved a distance Δs, and the resulting focal position is where the two red dashed lines converge, slightly below the original position of the bead. This derivation is based on a similar one presented in [1] but adds the extra layer of the polystyrene dish in the light path.

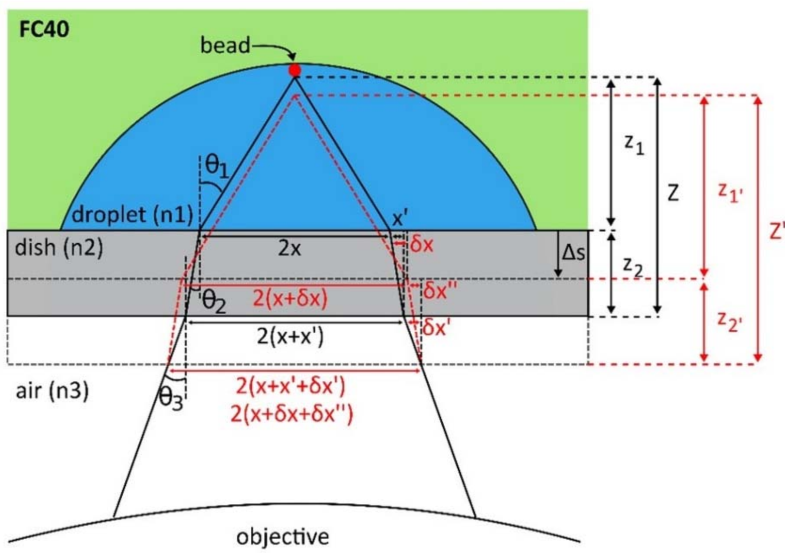

Fig. S10. Correcting focal shift when measuring conduit height on inverted microscopes. A drop of medium (which contains fluorescent beads and is overlaid with FC40) sits on a polystyrene dish on the stage of an inverted microscope. One red fluorescent bead stuck to the medium:FC40 interface at the peak of the spherical cap is brought into focus. Moving the stage a distance Δs closer to the objective moves the focus below the bead by a distance $\Delta f \neq \Delta s$ due to refraction of the light path across the different substrates. Using a combination of Snell's law and geometry, the correct value of Δf is determined using the numerical aperture of the objective lens, the refractive index of the culture medium around the bead, and the refractive index of the air at the objective, as in Eq. S40.

The marginal rays of the light cone emerging from the bead hit the dish at angle $\theta 1$, and have a half-width of x. Rays then travel through the dish at angle $\theta 2$ and emerge from the dish into air at angle $\theta 3$ with a new half-width of $x + x'$, before entering the objective. As the microscope stage is moved, we can see that the angles of the rays stay the same, while half-widths of light cones vary.

If the original depth of focus is Z, and moving the microscope stage results in a new depth of focus Z', then the axial focal shift is given by $Z' - Z$.

In Fig. S10, we have the relationships:

$$Z = z_1 + z_2$$
$$Z' = z_1' + z_2{}'$$

Using trigonometry, we determine the following relations:

$$tan(\theta_1) = \frac{x}{z_1} \equiv z_1 = \frac{x}{tan(\theta_1)}$$

$$tan(\theta_2) = \frac{x'}{z_2} \equiv z_2 = \frac{x'}{tan(\theta_2)}$$

$$tan(\theta_1) = \frac{x + \delta x}{z_1{}'} \equiv z_1{}' = \frac{x + \delta x}{tan(\theta_1)}$$

$$tan(\theta_2) = \frac{\delta x''}{z_2{}'} \equiv z_2{}' = \frac{\delta x''}{tan(\theta_2)}$$

$$tan(\theta_3) = \frac{\delta x'}{\Delta s} \equiv \delta x' = \Delta s \times tan(\theta_3)$$

As the thickness $z2$ of the dish does not change, then:

$$z_2 = z_2' \rightarrow \frac{x'}{tan(\theta_2)} = \frac{\delta x''}{tan(\theta_2)} \rightarrow x' = \delta x''$$

Furthermore, we can see from the half-width of the light cone emerging from the dish after the stage has moved that:

$$x + x' + \delta x' = x + \delta x + \delta x''$$

$$\rightarrow x + x' + \delta x' = x + \delta x + x'$$

$$\therefore \delta x' = \delta x = \Delta s \times tan(\theta_3)$$

The focal shift is therefore:

$$\Delta f = Z' - Z = z_1' + z_2' - z_1 - z_2$$

$$\Delta f = z_1' - z_1 = \frac{x + \delta x}{tan(\theta_1)} - \frac{x}{tan(\theta_1)}$$

$$\Delta f = \frac{\delta x}{tan(\theta_1)}$$

$$\therefore \Delta f = \Delta s \frac{tan(\theta_3)}{tan(\theta_1)}$$

This can now be expressed in terms of the numerical aperture of the objective, NA:

$$NA = n1 \times sin(\theta_1) \leftrightarrow \theta_1 = sin^{-1}\left(\frac{NA}{n1}\right)$$

Therefore:

$$\Delta f = \Delta s \frac{\tan\,(sin^{-1}\left(\frac{NA}{n3}\right)}{\tan\,(sin^{-1}\left(\frac{NA}{n1}\right)} \qquad (S40)$$

For small NA, we use the small-angle approximation:

$$sin(\theta) = \theta, tan(\theta) = \theta$$

and:

$$\Delta f = \Delta s \frac{tan\left(\frac{NA}{n3}\right)}{tan\left(\frac{NA}{n1}\right)} = \Delta s \frac{n1}{n3}$$

To confirm the accuracy of Eq. S40 for height corrections, we measured the heights of sessile drops of known volumes with the Olympus microscope. Droplets of 0.5 and 1 µL were deposited on polystyrene culture dishes, made from the same media + bead mixture used to measure conduit heights. As before, the diameter and heights of drops were measured, theoretical heights determined using the known volume and measured footprint. The heights measured using beads were then corrected using Eq. S40 and show good agreement with theory (using the height-to-volume equation for sessile drops [2]; average of 2% difference between theoretical and corrected heights across 21 individual measurements; Table S2).

Table S2. Comparison between sessile-drop height measurements and theoretical predictions using Eq. S40

drop volume (μL)	footprint diameter (mm)	measured height (mm)	theoretical height (mm)	corrected height (mm)	ratio corrected vs theoretical
0.5	1.666	0.294	0.422	0.427	1.012
	1.670	0.278	0.421	0.404	0.960
	1.663	0.270	0.424	0.392	0.926
	1.667	0.287	0.422	0.417	0.989
	1.678	0.295	0.418	0.429	1.026
	1.685	0.290	0.415	0.421	1.016
	1.680	0.262	0.417	0.381	0.913
	1.687	0.252	0.414	0.366	0.884
	1.696	0.273	0.411	0.397	0.966
1	2.058	0.368	0.549	0.535	0.974
	2.078	0.377	0.541	0.548	1.013
	2.101	0.370	0.532	0.538	1.012
	2.136	0.376	0.518	0.546	1.056
	2.134	0.345	0.518	0.501	0.967
	2.136	0.334	0.518	0.485	0.938
	2.165	0.315	0.506	0.458	0.904
	2.157	0.350	0.509	0.509	0.999
	2.167	0.338	0.506	0.491	0.972
	2.113	0.363	0.527	0.528	1.001
	2.126	0.350	0.521	0.509	0.975
	2.138	0.370	0.517	0.538	1.040

Maintaining constant shear along fluid-walled conduits

For conduits with chokes, the profile of both choke and conduit are determined using Eq. 2. While the exit height of the choke can be assumed to be zero, the conduit-choke junction determines conduit exit height ($x_{conduit} = 0$) as this will naturally be larger than the choke's starting height ($x_{choke} = L_{choke}$). We assume the transition between the choke start to conduit exit is small so the Laplace pressure is constant, and that the pressure-head difference due to FC40 is negligible; then, we equate the Laplace pressure in both regions such that $\Delta P_{conduit(x\,=\,0)} = \Delta P_{choke(x\,=\,L)}$ and hence $R_{conduit(x\,=\,0)} = R_{choke(x\,=\,L)}$. As the radius of curvature $R = \frac{a^2+h^2}{2h}$, we solve for conduit starting-height yielding:

$$h_{conduit(x\,=\,0)} = \frac{a_{choke}^2 + h_{choke(x=L)}^2 - \sqrt{\left(a_{choke}^2 + h_{choke(x=L)}^2\right)^2 - 4a_{conduit}^2 h_{choke(x\,=\,L)}^2}}{2h_{choke(x=L)}}$$

Here, a is fixed and defined when printing the conduit, and $h_{choke(x=L)}$ is the height of the choke before the junction and is calculated from the semi-analytical solution. Since the junction has a saddle shape, for conduits in Fig. 4B,C, the height of the choke, $h_{choke(x=L)}$, is taken at a distance away from the junction equivalent to one choke width (e.g., for choke width = 400 µm, $L_{choke} = 10$ mm, $h_{choke(x=L)} = 9.6$ mm). For conduits with geometries where $a_{conduit} \gg h_{conduit}$ and $a_{choke} \gg h_{choke}$, the radius of curvature is simplified to $R = \frac{a^2}{2h}$ and thus:

$$h_{conduit(x\,=\,0)} = \frac{a_{conduit}^2 h_{choke(x\,=\,L)}}{a_{choke}^2}$$

In this case, introducing a choke has the effect of increasing $h_{conduit}$ proportionately to $\frac{a_{conduit}^2}{a_{choke}^2}$, and maintains the conduit at an approximately constant height upstream of the choke due to the small pressure drop.

Semi-analytical solution for shear stress

We evaluate the wall shear stress at any location along conduit length and any z-location across its width. Starting from Eq. S6 and substituting u_{max} with Eq. S10 yields:

$$u_{max(z)} = \frac{Q{h_z}^2}{0.6{h_{max}}^3 a} \tag{S41}$$

Since $\tau = \mu \frac{du}{dy}$, and differentiating $u(y) = \left(1 - \frac{4y^2}{h_{max}^2}\right) u_{max}$ to obtain $\frac{du}{dy} = \frac{8y}{h_{max}^2} u_{max}$, we express the shear stress in the conduit as:

$$\tau_{max(z)} = \frac{8\mu y}{{h_z}^2} u_{max(z)} \tag{S42}$$

Substituting $u_{max(z)}$ from Eq. S41 into Eq. S42 we get:

$$\tau_{max(z)} = \frac{8Q\mu}{0.6{h_{max}}^3 a} y$$

Wall shear stress is evaluated at $y = \frac{h_z}{2}$ hence:

$$\tau_{max(z)} = \frac{4Q\mu h_z}{0.6{h_{max}}^3 a} \tag{S43}$$

At the conduit centre ($z = 0$), $h_z = h_{max}$, therefore Eq. S43 becomes:

$$\tau_{max(0)} = \frac{4Q\mu}{0.6h_{max}^2 a} \tag{S44}$$

Expressing $\tau_{max(z)}$ in terms of $\tau_{max(0)}$ using Eq. S44:

$$\tau_{max(z)} = \tau_{max(0)} \frac{h_z}{h_{max}} \tag{S45}$$

Now evaluating τ_{max} by substituting h_{max} with Eq. S20 finally yields:

$$\tau_{max(z)} = 1.28\sqrt{\frac{\mu\gamma Q}{a^3 x}} \frac{h_z}{h_{max}} \tag{S46}$$

Effect of a choke on the gradient of wall shear stress

The addition of a choke creates a region of nearly uniform shear upstream of the choke (i.e., $\frac{d\tau}{dx}$ is very small). This shear distribution would be achieved in a conduit without choke, but at a much farther distance. The choke allows users to 'skip ahead' through a conduit to reach a desired shear stress distribution. Conduits with small $\frac{d\tau}{dx}$ can be obtained at operational scales (that fit in 60 mm dishes) that would require much longer lengths of conduit otherwise. To investigate the order-of-magnitude effect of a choke on $\frac{d\tau}{dx}$, consider the two systems in Fig. S11.

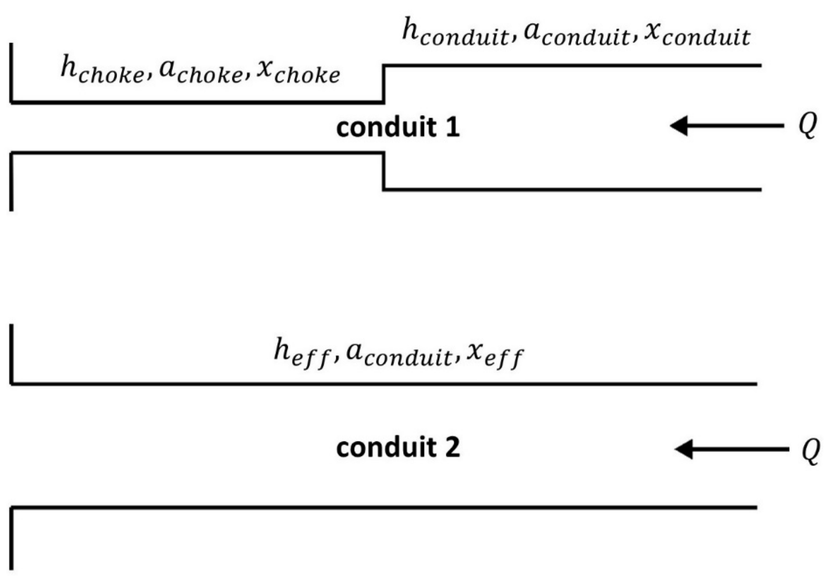

Fig. S11. Conduits with and without a choke. Both conduits are perfused at the same flow rate Q, and $a_{conduit}$ in conduit 1 is equivalent to $a_{conduit}$ in conduit 2.

Due to the choke in conduit 1, $h_{conduit} \approx h_{choke}\left(\frac{a_{conduit}}{a_{choke}}\right)^2$. From our semi-analytical equation:

$$h_{choke} = \left(\frac{26.08Q\mu a_{choke}x_{choke}}{\gamma}\right)^{0.25}$$

$$\therefore h_{conduit} \approx \left(\frac{26.08Q\mu a_{choke}x_{choke}}{\gamma}\right)^{0.25}\left(\frac{a_{conduit}}{a_{choke}}\right)^{2} \qquad (S47)$$

Next, for the same flow rate we determine the distance x_{eff} that conduit 2 (which has width $a_{conduit}$) would need to reach so that $h_{eff} = h_{conduit}$ at the junction between conduits (i.e., the effective length introduced by the choke):

$$\left(\frac{26.08Q\mu a_{conduit}x_{eff}}{\gamma}\right)^{0.25} = \left(\frac{26.08Q\mu a_{choke}x_{choke}}{\gamma}\right)^{0.25}\left(\frac{a_{conduit}}{a_{choke}}\right)^{2}$$

$$a_{conduit}x_{eff} = a_{choke}x_{choke}\left(\frac{a_{conduit}}{a_{choke}}\right)^{8}$$

$$\therefore x_{eff} = x_{choke}\left(\frac{a_{conduit}}{a_{choke}}\right)^{7} \qquad (S48)$$

As an example, if $x_{choke} = 1$ mm, $a_{choke} = 0.2$ mm, and $a_{conduit} = 0.5$ mm, then $x_{eff} = 0.6$ m.

Next, we evaluate the relationship between $\frac{d\tau}{dx}$ and the distance x along the conduit. Shear stress in the conduit ($@h_{max(x)}$) is:

$$\tau = 1.28\left(\frac{Q\mu\gamma}{a^3x}\right)^{0.5} \qquad (S49)$$

$$\therefore \tau \propto \left(\frac{1}{a^3x}\right)^{0.5}$$

As:

$$\frac{d}{dx}\left(\left(\frac{1}{a^3x}\right)^{0.5}\right) = -\frac{1}{2}a^3\left(\frac{1}{a^3x}\right)^{\frac{3}{2}}$$

Then:

$$\frac{d\tau}{dx} \propto a^3\left(\frac{1}{a^3x}\right)^{\frac{3}{2}} \propto \left(\frac{1}{ax}\right)^{\frac{3}{2}} \qquad (S50)$$

Using Eq. S48, the shear gradient after the choke is:

$$\left(\frac{d\tau}{dx}\right)_{choke} \propto \left(\frac{1}{a_{conduit}x_{eff}}\right)^{\frac{3}{2}} \propto \left(\frac{1}{a_{conduit}x_{choke}\left(\frac{a_{conduit}}{a_{choke}}\right)^{7}}\right)^{\frac{3}{2}} \qquad (S51)$$

The shear gradient for a conduit without choke at x_{choke} is:

$$\left(\frac{d\tau}{dx}\right)_{no\ choke} \propto \left(\frac{1}{a_{conduit}x_{choke}}\right)^{\frac{3}{2}} \tag{S52}$$

Hence, the change in $\frac{d\tau}{dx}$ from the addition of a choke can be evaluated as:

$$\frac{\left(\frac{d\tau}{dx}\right)_{no\ choke}}{\left(\frac{d\tau}{dx}\right)_{choke}} \equiv \frac{\left(\frac{1}{a_{conduit}x_{choke}}\right)^{\frac{3}{2}}}{\left(\frac{1}{a_{conduit}x_{choke}\left(\frac{a_{conduit}}{a_{choke}}\right)^{7}}\right)^{\frac{3}{2}}} \equiv \left(\frac{a_{conduit}}{a_{choke}}\right)^{\frac{21}{2}} \tag{S53}$$

In our example, $\frac{d\tau}{dx}$ in the conduit after the choke will be ~ 15000 fold smaller than $\frac{d\tau}{dx}$ in the straight conduit at the same distance from the exit (equivalent to a 99.99% decrease). Table S3 gives the percent change in τ over 1 cm upstream of a choke, for various choke lengths and $\frac{a_{conduit}}{a_{choke}}$ ratios.

Table S3. % change in τ over 1 cm for varying half-width ratios and choke lengths

$\frac{a_{conduit}}{a_{choke}}$	% change in τ over 1 cm with choke length of:		
	1 mm	**5 mm**	**10 mm**
2.5	0.81	0.16	0.08
2	3.69	0.77	0.39
1.25	43.18	16.07	9.08
1	69.85	42.26	29.29

Error from $\frac{h}{a}$ simplification on shear stress gradient in choked conduits

The height of a conduit after a choke is estimated without simplifications as:

$$h_{conduit(exact)} = \frac{a_{choke}^2 + h_{choke}^2 - \sqrt{(a_{choke}^2 + h_{choke}^2)^2 - 4a_{conduit}^2 h_{choke}^2}}{2h_{choke}} \tag{S54}$$

However, Eq. S54 is simplified when assuming the radius of curvature is expressed as $R = \frac{a^2}{2h}$, yielding:

$$h_{conduit(simp)} = h_{choke}\left(\frac{a_{conduit}}{a_{choke}}\right)^2 \tag{S55}$$

The error or difference from this simplification is given as:

$$\frac{h_{conduit(exact)}}{h_{conduit(simp)}} = c \qquad (S56)$$

where c is a constant dependent on h_{choke}, a_{choke}, and $a_{conduit}$. From Eq. S55, the effective length introduced by the choke is determined (as in Eq. S48):

$$x_{eff(simp)} = x_{choke}\left(\frac{a_{conduit}}{a_{choke}}\right)^7 \qquad (S57)$$

Introducing Eq. S57 into the expression for wall shear stress (Eq. S49) yields:

$$\tau_{simp} = 1.28\left(\frac{Q\mu\gamma}{a^3 x_{eff}}\right)^{0.5} \qquad (S58)$$

The radius of curvature simplification from Eq. S55 introduces an error (c) in Eq. S58; this is accounted for using Eq. S56, such that x_{eff} and τ become:

$$x_{eff(corrected)} = x_{choke}c^4\left(\frac{a_{conduit}}{a_{choke}}\right)^7 \qquad (S59)$$

$$\tau_{corrected} = 1.28\left(\frac{Q\mu\gamma}{a^3 x_{eff(corrected)}}\right)^{0.5} \qquad (S60)$$

Finally, as in Eq. S44, τ may also be expressed in terms of conduit height rather than effective length, using the exact (Eq. S54) or simplified equation (Eq. S55). The exact expression using Eq. S54 is:

$$\tau_{exact} = \frac{4Q\mu}{0.6h^2_{conduit(exact)}a_{conduit}} \qquad (S61)$$

As shear stress in Fig. 4D is calculated using Eq. S61, we evaluate the effect of the radius of curvature simplification on τ (Eq. S58), and subsequent correction (Eq. S60), for the choked conduits in Fig. 4B. Table S4 summarizes the estimated % change in τ for these conduits over 1 cm upstream of the choke, showing equivalent results for Eq. S60 and S61.

Table S4. Effect of h/a simplification on τ predictions

choke length	1 mm	5 mm	10 mm
$h_{conduit(exact)}$ (Eq. S54) [µm]	157	287	322
$h_{conduit(simp)}$ (Eq. S55) [µm]	152	220	237
c (Eq. S56)	1.03	1.31	1.36
$x_{eff(simp)}$ (Eq. S57) [m]	0.58	2.54	3.28
$x_{eff(corrected)}$ (Eq. 59) [m]	0.66	7.39	11.19
τ_{simp} @ choke (Eq. S58) [Pa]	9.76E-04	4.65E-04	3.87E-04
τ_{simp} @ 1 cm (Eq. S58) [Pa]	9.68E-04	4.64E-04	3.87E-04
$d\tau/dx$ 1cm (%)	0.85	0.20	0.15
$\tau_{corrected}$ @ choke (Eq. S60) [Pa]	9.13E-04	2.73E-04	2.10E-04
$\tau_{corrected}$ @ 1 cm (Eq. S60) [Pa]	9.06E-04	2.73E-04	2.10E-04
$d\tau/dx$ 1cm (%)	0.75	0.07	0.04
τ_{exact} @ choke (Eq. S61) [Pa]	9.31E-04	2.78E-04	2.14E-04
τ_{exact} @ 1 cm (Eq. S61) [Pa]	9.24E-04	2.78E-04	2.14E-04
$d\tau/dx$ 1cm (%)	0.75	0.07	0.04

Culturing cells in fluid-walled conduits

We plated human umbilical vein endothelial cells (HUVECs) in conduits (± choke) and perfused them overnight (at 25 or 50 µL/h) to look at the effect of flow on cell viability. Fig. S11 shows that after 24 h, flow had little effect on HUVEC morphology or alignment, which is to be expected from the magnitude of the shear stress in such conduits (see Fig. 4D) [3].

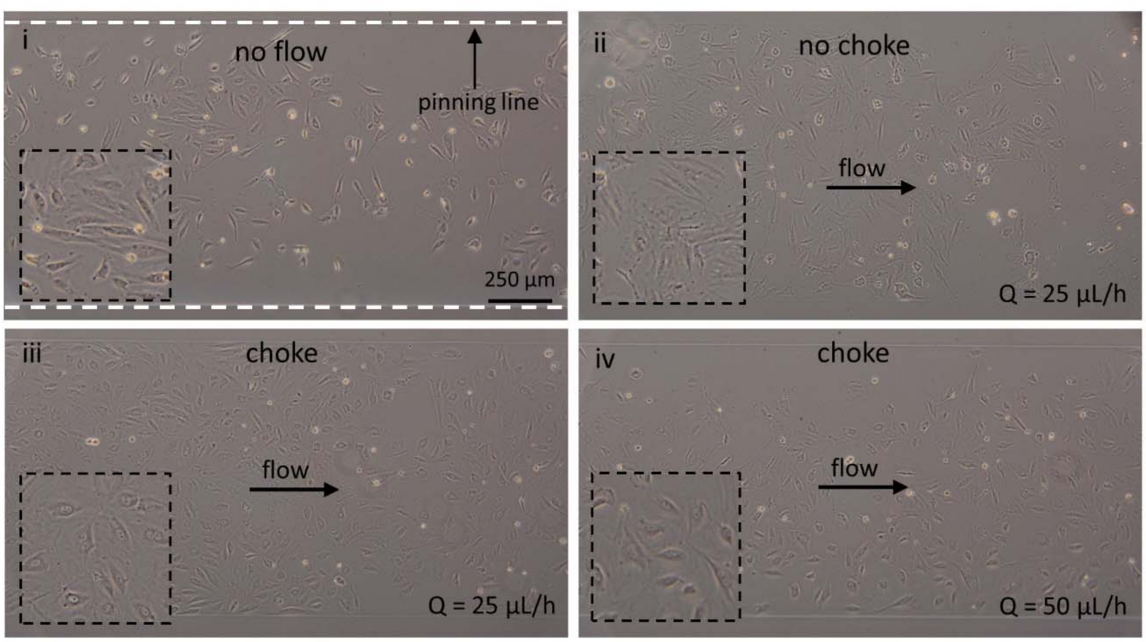

Fig. S12. HUVECs in fluid-walled conduits. Cells were plated in 4 conduits ± chokes (conduit width 1 mm; choke width 400 µm) and incubated overnight before flow was applied. Insets show close-ups of cells in conduits. **(i)** Control conduit without flow. White dashed lines indicate conduit pinning lines (triple contact line polystyrene-media-FC40). **(ii)** Conduit without choke, perfused at 25 µL/h. **(iii)** Conduit with choke, perfused at 25 µL/h. **(iv)** Conduit with choke, perfused at 50 µL/h.

Movie S1. Addition of FBS to DMEM immediately induces the no-slip condition
Two square chambers (1.9 x 1.9 mm) each containing 400 nL DMEM plus 4 mg/ml red dye (Allura Red in H_2O, Sigma) and 3-10 µm glass beads (1:1000 dilution, Polysciences, Inc., 07666) are each surrounded by FC40 walls; these chambers sit in a dish filled with FC40 on the Olympus microscope (4x objective). Next, the jetting needle (diameter 500 µm) – held vertically by attachment to the microscope condenser, filled with FC40, and connected to a syringe pump – is lowered through the fluorocarbon until ~1 mm above the footprint of the FC40 wall between the two chambers. This needle gives the circular shadow in the middle of video images. The movie begins as the pump is started and projects a submerged FC40 jet downwards at 8 µL/s; this induces shear at the FC40:medium interface so beads in both chambers swirl rapidly. After ~10 s, 0.5 µL DMEM + 10% FBS is manually pipetted into the bottom chamber; beads in the inoculated chamber rapidly stop moving, as those in the upper one continue. This shows that FBS immediately induces a no-slip interface.

SI References

[1] T. D. Visser, J. L. Oud, and G. J. Brakenhoff, "Refractive index and axial distance measurements in 3-D microscopy," *Optik (Stuttg).*, vol. 90, no. 1, pp. 17–19, 1992.

[2] E. J. Walsh *et al.*, "Microfluidics with fluid walls," *Nat. Commun.*, vol. 8, no. 1, p. 816, 2017, doi: 10.1038/s41467-017-00846-4.

[3] J. Shemesh, I. Jalilian, A. Shi, G. Heng Yeoh, M. L. Knothe Tate, and M. Ebrahimi Warkiani, "Flow-induced stress on adherent cells in microfluidic devices," *Lab Chip*, vol. 15, no. 21, pp. 4114–4127, 2015, doi: 10.1039/C5LC00633C.